Imaging the seismic velocity structure of the crust and upper mantle in the northern East African Rift using Rayleigh wave tomography

Emma L. Chambers[1], Nicholas Harmon[1], , Catherine A. Rychert[1], Ryan J. Gallacher[1,3] and Derek Keir[1,2]

[1)] University of Southampton, Southampton, UK
[2)] Dipartimento di Scienze della Terra, Università degli Studi di Firenze, Florence, Italy
[3)] Department of Earth and Environmental Sciences, Tulane University, New Orleans, USA

This manuscript has been accepted for publication in Geophysical Journal International. It has undergone peer-review and was accepted on 14/04/2022 and available online on 22/04/2022. The manuscript is the unformatted accepted version. The final version of the manuscript is available via the 'Peer-reviewed Publication DOI link on the right hand side of this webpage and at: https://doi.org/10.1093/gji/ggac156 .

The final shear velocity model is available at https://doi.org/10.5258/SOTON/D1408 .

The paper should be cited as:

"Emma L Chambers, Nicholas Harmon, Catherine A Rychert, Ryan J Gallacher, Derek Keir, Imaging the seismic velocity structure of the crust and upper mantle in the northern East African Rift using Rayleigh wave tomography, *Geophysical Journal International*, 2022;, ggac156, https://doi.org/10.1093/gji/ggac156"

Please feel free to contact any of the authors; we welcome feedback.

Imaging the seismic velocity structure of the crust and upper mantle in the northern East African Rift using Rayleigh wave tomography

Emma L. Chambers[1,2], Nicholas Harmon[1], Catherine A. Rychert[1], Ryan J. Gallacher[3,4] and Derek Keir[1,5]

[1)] University of Southampton, Southampton, UK

[2)] Dublin Institute for Advanced Studies, Dublin, Ireland

[3)] International Seismological Centre, Pipers Lane, Thatcham, Berkshire, RG19 4NS, UK

[4)] Department of Earth and Environmental Sciences, Tulane University, New Orleans, USA

[5)] Dipartimento di Scienze della Terra, Università degli Studi di Firenze, Florence, Italy

Corresponding author: Emma L. Chambers (echambers@cp.dias.ie)

Summary

Understanding the dynamics and evolution of continental rifting is broadly important for our understanding of plate tectonics. The northern East African Rift offers an excellent opportunity to study these processes at an active rift that was initiated by a large magmatic event. Multiple seismic models have been produced to understand the evolution of magmatism which image punctuated slow velocity zones in the asthenosphere. However, the depth extent of the slow velocity bodies has been less well constrained leading to much debate regarding the primary controls on melt generation. Variations between methods, resolution, and scale of the seismic models make direct quantitative comparisons challenging. The lack of instrumentation off-rift further limits our understanding of the spatial extent of tectonic and magmatic processes, which is crucial to understanding magmatic continental rifting. In this paper, we jointly invert Rayleigh wave dispersion curves from ambient noise and teleseisms to obtain absolute shear velocity maps at 10–150 km depth. This includes data

from a new seismic network located on the Ethiopian Plateau and enhanced resolution at Moho and upper mantle depths from the joint inversion. At crustal depths, velocities are slowest beneath the Main Ethiopian Rift and the off-rift Ethiopian Plateau (<3.00-3.75 ±0.04 km/s, 10–40 km depth) and ongoing magmatic emplacement is required. At 60–80 km depth off-rift, we observe a fast velocity lid (>0.1 km/s faster than surroundings), in agreement with previous estimates of lithospheric thickness from receiver functions. The fast lid is not observed within the Main Ethiopian Rift or central Afar which instead are underlain by asthenospheric slow velocity anomalies (<4.05 ±0.04 km/s at 60–120 km depth). This suggests melt is infiltrating the lithosphere within the rift. Furthermore, punctuated asthenospheric slow velocity anomalies (~110x80 km wide) exist in areas that have not undergone significant crustal and plate thinning, potentially indicating melt infiltration may start prior to significant plate deformation. Finally, the punctuated asthenospheric slow velocity zones are not located directly beneath melt-rich crustal regions including those off-rift, suggesting melt migration processes are dynamic and/or may occur laterally.

Key words: Seismology - Joint inversion - Seismic tomography - Africa - Surface waves and free oscillations

1.0 Introduction

Continental rifting is a fundamental component of plate tectonics that has shaped the geological record. Yet understanding the mechanisms and processes of continental rifting is often obscured by the complex geology left behind in ancient rifts, and only a few tectonically active rifts are available for study in the present day. The northern East African Rift (EAR), is a primary example of a tectonically active magma-assisted rift (e.g. Ebinger & Casey, 2001; Mackenzie et al., 2005). In this end-member style of rift, magma injection weakens the relatively strong continental lithosphere, and allows tectonic forces to extend the plate (e.g. Buck, 2006; Koptev et al., 2018; Rooney et al., 2014) (Figure 1). Models and geological observations of magmatic continental rifting suggest melt production and localised emplacement occur beneath the rift valley (Buck, 2006; Corti et al., 2015; Keir et al., 2012; Rooney et al., 2005, 2014). Recent velocity models also observe punctuated slow velocity zones in the upper asthenosphere, though their cause and extent, both in time and space, are debated. Crucially, many studies have focused to the rift valley and rift flanks with less attention paid to the off-rift regions. Key information about the character of the off-rift lithosphere and asthenosphere structure, and the relationship to the lithosphere-asthenosphere system within the rift, combined with the location and migration of melt, is needed to fully understand plate extension. Below we detail the pertinent information about the northern EAR system, to motivate our present study using Rayleigh wave tomography, in order to characterise the unrifted flanks and rifts and better understand these relationships.

1.1 Geological Background

Precambrian basement, formed during the Neoproterozoic Pan-African orogeny, underlies much of Ethiopia and the surrounding area (Mège & Korme, 2004). Volcanism initiated 45-40 Ma and continues to the present day, with the first eruptions beneath the Amaro province

of southern Ethiopia (Davidson & Rex, 1980; Ebinger et al., 1993; George et al., 1998; Rooney, 2017). The largest volcanic event was the emplacement of the Ethiopian flood basalt province, occurring 31-29 Ma (Hofmann, et al., 1997; Rooney, et al., 2012a; Ukstins et al., 2002) with sporadic volcanism continuing on the Ethiopian Plateau, including the emplacement of alkali shield volcanoes above the flood basalts (e.g. Choke and Guguftu 22 Ma (Kieffer et al., 2004)). Volcanic activity today is largely focused within ~15 km-wide and 60 km-long crustal magmatic segments at the rift axis which are oblique to the border faults and trend en-echelon along the rift (Ebinger et al., 2001; Wolfenden et al., 2004) (Figure 1). Recent volcanism has occurred off-rift at Nabro volcano in Afar (Goitom et al., 2015), in the Yerer-Tullu Wellel Volcanotectonic Lineament (YTVL) (Rooney et al., 2014) and eruptive centres are present south of Lake Tana (Corti, 2009; Kieffer et al., 2004) (Figure 1). The volcanic segments in Afar and the Main Ethiopian Rift (MER) are the main focus of present day extension, while prior to the Pleistocene, extension was focused at the border faults (Ebinger et al., 2001; Wolfenden et al., 2004, 2005).

Rifting in Afar initiated between 29 Ma (Wolfenden et al., 2004) and 26 Ma (Bosworth et al., 2005), just after the main flood basalt emplacement at 31-29 Ma (Hofmann et al., 1997; Pik et al., 1998; Wolfenden et al., 2004), while the MER started rifting later at 20 Ma in the south, and 11 Ma in the north (Wolfenden et al., 2004). Extension rates are variable with full spreading rates of ~6 mm/yr for the MER (Birhanu et al., 2016; Jestin et al., 1994; Saria et al., 2014), 16 mm/yr for the Gulf of Aden Rift (Jestin et al., 1994; Vigny et al., 2006) and 18 mm/yr for the Red Sea Rift (McClusky et al., 2010; Vigny et al., 2006) (Figure 1a). The Tendaho Goba'ad discontinuity (TGD) separates the east-west directed extension in the northern-most MER from the northeast-southwest directed extension in Afar (Tesfaye et al., 2003).

1.2 Geophysical constraints on the crust

The crust beneath the region has been modified by rifting and magmatism both in terms of thickness and composition. The crust is 35–40 km thick beneath the Somalian Plateau (Mackenzie et al., 2005; Stuart et al., 2006) and 30–35 km thick beneath the western edge of the Ethiopian Plateau (Ogden et al., 2019). These crustal thicknesses are likely representative of pre-rifted unmodified crust (Mackenzie et al., 2005; Ogden et al., 2019; Stuart et al., 2006). In contrast, crustal thickness for the eastern part of the Ethiopian Plateau ranges from 40-45 km, with the additional crust commonly interpreted to be several kilometres of magmatic addition from the flood basalt volcanism and likely associated lower crustal intrusions (Mackenzie et al., 2005; Ogden et al., 2019; Stuart et al., 2006; Wang et al., 2021).

Crustal thicknesses beneath the rift vary from <16 to 38 km with variable internal structure. Beneath the MER the crust is predominantly thinner than the plateaus at 25-35 km thick, with the exception of the southern MER, where crustal thickness ranges from 30-38 km (Hammond et al., 2011; Mackenzie et al., 2005; Ogden et al., 2019). Receiver function and active source tomography studies observe multiple discontinuity boundaries and faster velocities at lower crustal depths within the rift, providing evidence for magmatic intrusions (Hammond et al., 2011; Lavayssière et al., 2018; Maguire et al., 2006; Stuart et al., 2006; Wang et al., 2021). In Afar, crustal thickness ranges from <16-26 km, with the Danakil depression having the thinnest crust of the subaerial rift system (Dugda et al., 2005; Hammond et al., 2011; Makris & Ginzburg, 1987). Tomographic P-wave studies at crustal depths for both the MER and Afar image fast velocities which have previously been interpreted as cooled gabbroic intrusions (Daly et al., 2008; Mackenzie et al., 2005; Maguire et al., 2006) which is further corroborated by gravity studies (e.g. Cornwell et al., 2006). S-

wave and surface wave velocity studies, which are more sensitive to fluids, observe slow velocities in the MER and Afar suggesting a fluid component, in contrast to P-wave studies (Chambers et al., 2019; Keranen et al., 2009; Kim et al., 2012; Korostelev et al., 2015). Vp/Vs ratios for the crust are high within the rift (Daly et al., 2008), and in places >1.9, which have been interpreted as fluids and melt emplacement beneath the rift (Dugda et al., 2005; Hammond, et al., 2011; Ogden et al., 2019; Stuart et al., 2006). Magnetotelluric surveys observe high conductivity bodies within the crust beneath the rift and favour a similar interpretation of fluids and melt (Samrock et al., 2018; Whaler & Hautot, 2006).

SKS splitting studies of azimuthal anisotropy (Keir et al., 2011; Kendall et al., 2005), coupled with surface wave studies that constrain radial (Chambers et al., 2021), or radial and azimuthal anisotropy (Bastow et al., 2010), provide evidence for both dykes and sills in the lithosphere. Within the MER anisotropic receiver function and local earthquake splitting results show the largest amounts of anisotropy in the rift (Hammond, 2014), and surface waves make similar observations which were interpreted as oriented melt pockets (Bastow et al., 2010; Chambers et al., 2021). In Afar, anisotropic studies suggest a larger contribution from dyke intrusions and vertical cracks than the MER (Hammond, 2014; Keir et al., 2011). These observations taken together have previously been interpreted as evidence for rift aligned melt pockets within the crust and lithospheric mantle (Bastow et al., 2010; Chambers et al., 2021; Hammond, 2014).

Off-rift, there is similar evidence for ongoing lower crustal intrusions and magmatic activity. S-wave studies beneath the eastern part of the Ethiopian Plateau, Yerer Tullu Wellel Volcanotectonic lineament (YTVL) and the recent Nabro volcanic eruption (erupted 2011, Goitom et al., 2015), are characterised by slow velocities (Bastow et al., 2005; Chambers et

al., 2019; Keranen et al., 2009; Kim et al., 2012), coupled with high conductivity bodies beneath the YTVL (Whaler & Hautot 2006). A recent radial anisotropy study found evidence for alternating sill and country rock in the off-rift crustal structure (Chambers et al., 2021), while GPS measurements find evidence for ongoing extension off-rift (Birhanu et al., 2016).

1.3 Geophysical constraints on the mantle lithosphere and asthenosphere

Receiver functions have been used to constrain lithospheric thickness across the region. For instance, S-to-P receiver functions image negative phases interpreted as the lithosphere-asthenosphere-boundary (LAB) at 60-80 km depth beneath the Ethiopian Plateau, whereas beneath the MER and Afar, S-to-P does not find significant negative LAB discontinuities (Lavayssière et al., 2018; Rychert et al., 2012). The lack of a strong LAB phase could be consistent with either a very gradual velocity decrease with depth, or the lack of a fast mantle lithosphere (e.g. Fischer et al., 2020). Given that thermal gradients with depth are not likely to be very gradual in a rifting environment, the mantle lithosphere was interpreted as missing (Rychert et al., 2012) or very thin (<~10 km) (Lavayssière et al., 2018), which would make detection by S-to-P receiver functions difficult (Rychert & Harmon, 2018; Rychert et al., 2020). A joint inversion of Rayleigh wave group velocities and P-to-S receiver functions found similarly thick lithosphere beneath the plateau and virtually no fast lithospheric lid beneath the MER and Afar (Dugda et al., 2007). Beneath two stations in Afar the study found a thin (~10 km) layer at 40–50 km depth with a shear velocity of ~4.1 km/s that was interpreted as the mantle lithosphere.

Previous studies that considered surface waves or jointly considered surface waves and receiver functions suggest the upper mantle in the region is slow, both on and off-rift, with Vs = 3.80-4.25 km/s (Gallacher et al., 2016; Keranen et al., 2009). These velocities are

substantially slower than those observed at similar depths beneath continental interiors, where shear velocities are typically >4.45 km/s (Kennett et al., 1995). The area is also characterised by Vp values that are 4–10% slower than the global mean (Bastow et al., 2008, 2005; Boyce et al., 2021; Fishwick, 2010). One explanation for the observed slow velocities are elevated mantle potential temperatures where petrological modelling suggested values elevated by 100–170°C beneath the northern EAR (Ferguson et al., 2013; Rooney et al., 2012b). While elevated temperatures may account for off-rift velocities (e.g. Gallacher et al., 2016; Rooney et al., 2012b), velocities beneath the rift require another component such as a small amount of partial melt (Bastow et al., 2010, 2005; Chambers et al., 2019; Gallacher et al., 2016; Hammond et al., 2013).

At mantle depths, the slow velocities bodies are not continuous, but punctuated in character in regional and local scale studies (e.g. Bastow et al., 2005; Civiero et al., 2015, 2016; Gallacher et al., 2016; Hammond et al., 2013). Body wave tomography studies find evidence for punctuated slow velocity anomalies at asthenospheric depths, beneath and off set from the rift (Bastow et al., 2008, 2005). A teleseismic surface wave study by Gallacher et al. (2016) also found punctuated slow velocity zones, although did not observe the offset from the rift in the upper mantle, possibly due to lower horizontal resolution when compared to body waves. They interpreted these slow velocity zones as segmented buoyancy driven upwellings.

1.4 Motivation

In summary, the northern EAR (Figure 1) has been extensively imaged creating multiple velocity models at a range of depths (e.g. Bastow et al., 2008, 2005; Civiero et al., 2015; Keranen et al., 2004; Kim et al., 2012). A common feature of the models that image the mantle (e.g. Bastow et al., 2008, 2005; Civiero et al., 2015; Gallacher et al., 2016) is the

presence of punctuated slow velocity zones in the asthenosphere, though their cause is debated, with interpretations ranging from mantle plumes or plumelets (Civiero et al., 2015; Hammond et al., 2013), to focused upwellings and/or decompressing melting resulting from mechanical thinning of the lithosphere (Bastow et al., 2008, 2005), to buoyancy driven mantle upwelling (Gallacher et al., 2016). The depth and lateral extent of the slow velocity bodies have been less well constrained leading to much debate regarding the primary controls on melt generation and whether the slow velocity zones are located solely beneath the rift (Gallacher et al., 2016), offset towards the rift flanks (Bastow et al., 2008), or located beneath both the rift and plateaus (Civiero et al., 2015, 2016). In addition, melt migration pathways between the mantle and crust, and the nature of crustal magma storage are not well-known and consequently debated. At lower crustal depths and uppermost mantle depths, melt may be stored at the rift scale (Jin et al., 2015; Smith 1994), or as more isolated bodies throughout the full crust (Cashman et al., 2017; Hübert et al., 2018). Finally, we have fewer constraints on the off-rift characteristics. Off-rift – on-rift comparisons are likely important for our understanding of pre-rift conditions and the evolution of the rift, as is the possibility that magmatic processes occur over a broader region outside the rift valley.

A comprehensive view requires large scale tomographic imaging at high resolution for the lithosphere and asthenosphere beneath both on- and off-rift regions. While many studies have focused on the rift valley, less attention has been paid to off-rift regions, particularly west of Lake Tana. Recent geodetic and geological studies suggest extension may be more broadly distributed than the topographic rift valley (e.g. Birhanu et al., 2016; Mège & Korme, 2004), making it critical to image the lithosphere and asthenosphere in this region to understand the subsurface magmatic and tectonic processes including variations in plate structure, melt generation and melt migration processes. In addition, quantitative comparisons between the

off-rift regions and on-rift regions were complicated to produce given the large range in methodologies, resolutions, spatial scales and assumptions between studies.

An example of variability in approach is demonstrated in the three ambient noise tomography (ANT) studies in the region (Chambers et al., 2019; Kim et al., 2012; Korostelev et al., 2015). One study presented group velocity maps between 7 - 28 s period and a full 3-D shear velocity model (Kim et al., 2012), another presented phase velocity maps from 9–25.5 s period (Korostelev et al., 2015), and a further study presented phase velocity maps from 8–33 s and a full 3-D shear velocity model (Chambers et al., 2019). Each study also covered a different region (Afar (Korostelev et al., 2015), central MER (Kim et al., 2012) and broader rifted regions (Chambers et al., 2019)). In addition, while the group and phase velocity maps give a general sense of lateral variability, they cannot be quantitatively compared due to the differing sensitivity/depth averaging of the methods. Therefore, quantitative comparisons among these studies and across the entire region are not possible.

A similar example can be given for body wave tomography studies. Previous body wave tomography in the region used relative arrival-time analysis (Bastow et al., 2008, 2005; Benoit et al., 2006; Hammond et al., 2013). This provides information relative to a regional, not global background mean making quantitative comparisons among these studies from different areas challenging. Furthermore, it is difficult to directly infer physical properties such as temperature and/or melt from these studies (e.g. Bastow, 2012).

To facilitate direct comparison of regions at a consistent resolution and velocity, we produce a comprehensive seismic velocity model by performing a joint inversion between Rayleigh wave dispersion curves from ambient noise and teleseisms and use this to determine whether

melt supply is ubiquitous or punctuated along the rift. In addition, our unified model of absolute shear velocity ranges from 10–150 km depth, and enables us to explore the possibility of melt and variations in the structure beneath the Ethiopian Plateau. Data is obtained from seismometers present from 1999-2017 located in Ethiopia, Yemen, Djibouti and Eritrea, allowing coverage of regions unaffected by rifting (e.g. west of the Ethiopian Plateau) to areas at incipient seafloor spreading (e.g. Afar). The joint inversion builds on the crustal S-wave models derived from ambient noise (Chambers et al., 2019) and teleseismic Rayleigh waves (Gallacher et al., 2016) beneath the rift and rift flanks. It provides increased resolution at lower crustal and uppermost mantle depths which would not be possible with ambient noise or teleseisms individually. Furthermore, we image the Ethiopian Plateau west of lake Tana and on the Somalian Plateau which have not been tomographically imaged at a resolution sufficient to detect individual melt sources at crustal and upper mantle depths up until now. An additional benefit of the joint inversion is that tighter constraints on shallow structures reduces related artefacts in deeper structures, thus improving resolution of deeper structures. The joint inversion also allows us to compare the presence/absence of slow velocity anomalies likely related to melt in the asthenosphere to those in the crust in a consistent manner to better constrain the pathways of melt and associated dynamics.

2.0 Methods

2.1 Datasets

We used data from 13 temporary seismic networks and 5 permanent stations installed between 1999 and 2017 (Figure 1a). We used the vertical component data from the broadband seismometer stations. Fifty-eight stations from 3 networks were included (ARGOS XM 2012-2014, Plateau YY 2014-2016 and Afar0911 2H 2012-2013), in addition to the 170 used in Chambers et al. (2019) and 290 in Gallacher et al. (2016) (Figure 1a). The

variation in the number of stations between the two studies arise from the 3λ station separation requirement for the ambient noise cross-correlations resulting in the removal of the RiftVolc (Y6 2016–2017) network. Furthermore, networks and stations with short deployment durations such as the EAGLE phase iii network, were not included in the ambient noise.

2.2 Ambient Noise Phase Velocity

2.2.1 Data Processing

The vertical component data was downsampled to 1Hz, normalised and whitened with a 4th order Butterworth bandpass filter between 0.005–0.4 Hz following the method of Bensen et al. (2007). The data were cross-correlated on the 24-hour long waveforms for each concurrently running station pair. The cross-correlograms for every day and each station pair were then stacked to improve the signal to noise ratio (SNR). Station pairs with less than 10 days of continuous recording, 10 days' worth of stacked cross-correlation functions, interstation distances <3λ or a SNR <3 were removed (Bensen et al., 2007; Chambers et al., 2019; Harmon et al., 2007) resulting in 34991 total cross-correlation functions and 6716 unique cross-correlation functions (Supplementary Figure S1). We examined the stability of the cross-correlations through time, and found that typically >1 month stacks produced waveforms with phases that were within 1-2 s of the long term stack. SNR increased as expected with longer time period stacks and is consistent with numerous previous studies (e.g. Bensen et al., 2007). Then the fundamental mode Rayleigh wave data were windowed using a time variable filter (Landisman et al., 1969), and the Fourier amplitude and phase calculated at each frequency of interest via a fast Fourier transform. For the ambient noise phase data we assign an *a priori* error (square root of the diagonals of Cnn, the data covariance matrix from the iterative damped least squares inversion) of 6% of a cycle.

2.2.2 1-D Phase Velocity

The phase velocity dispersion across the region was estimated using a spatial domain technique across the entire array. A zero order Bessel function of the first kind was fitted to the real part of the Noise Correlation Function (NCF) in the Fourier domain by searching over phase velocities from 2.5–5 km/s in 0.01 km/s steps for every period of interest (Aki, 1957). For each stacked NCF the phase was measured at each period by unwrapping the phase, using the average phase velocity curve at the longest periods, to resolve cycle ambiguity (Bensen et al., 2007; Harmon et al., 2008).

2.2.3 2-D Phase Velocity

The phase velocity maps were then generated by inverting the phase data using the Born approximation 2-D phase sensitivity kernels (Zhou et al., 2004) and an iterative damped least squares approach (Tarantola & Valette, 1982) using the equation:

$$\Delta \boldsymbol{m_i} = \left(\boldsymbol{G^T C_{nn}}^{-1}\boldsymbol{G} + \boldsymbol{C_{mm}}\right)^{-1} (\boldsymbol{G^T C_{nn}^{-1}} \Delta \boldsymbol{d} + \boldsymbol{C_{mm}^{-1}}[\boldsymbol{m_i} - \boldsymbol{m_0}]) \quad (1)$$

where m_i is the current model at iteration i, Δm_i is the change to the model after the next iteration, G is the matrix of partial derivatives from the kernel at each node (Saito, 1988), C_{nn} is the data covariance matrix, C_{mm} is the model covariance matrix, Δd is the difference between the observed and predicted phase, and m_0 is the starting model (Harmon et al., 2007; Tarantola et al., 1982). The final term ($\boldsymbol{C_{mm}^{-1}}[\boldsymbol{m_i} - \boldsymbol{m_0}]$) damps the model towards the initial model using the a priori model covariance.

We used a regular 0.25° x 0.25° grid of nodes as our parameterisation for the inversion (Figure 2) and averaged the sensitivity kernel between each station pair onto the nodes (Harmon et al., 2013; Yang & Forsyth, 2006). The sensitivity kernel is calculated at every period for each station pair on a densely sampled grid (0.1° x 0.1°) and then the Gaussian

distance-weighted average value is taken to determine the value at each node on the coarser grid with a Gaussian width (2-sigma) of 40 km. The inversion estimates the average phase velocity at each node, then we "undo" the Gaussian weighted average to recover a 0.1° x 0.1° sampled grid by determining the Gaussian weighted contribution of the nearest nodes to each pixel using the same 40 km Gaussian width which further smooths the kernels as well. We present the formal uncertainty from the last iteration of the inversion, which is propagated from the nodal parameterisation to the higher density grid using the Gaussian weights of each node at each pixel using the full covariance matrix. We used an a priori model covariance of 0.2 km/s^2 in the phase velocity inversion along the diagonals of C_{mm} (Supplementary Figure S3). This choice stabilises the inversion but is not restrictive as the value is much larger than the standard deviations from the mean velocity at each period (Forsyth & Li, 2005). Choices smaller than 0.2 km/s resulted in damped velocity variations. This resulted in well resolved phase velocity maps between 8-26 s which are indicated in the average 1-D profiles in Figure 3 and S4, with lower uncertainties in the rift and at shallower depths.

2.3 Teleseismic Rayleigh wave phase velocity

2.3.1 Data Processing

We extracted amplitude and phase information from vertical component seismograms for earthquakes with >5.5 magnitude and epicentral distances of 25-150° (1053 events, Figure 1 inset and supplementary Figure S1). For each teleseismic event, raw data were demeaned and detrended and their instrument response was removed. The data were then bandpass filtered using a 4th order Butterworth filter with corner frequencies between 0.005–0.4 Hz. Then the fundamental mode Rayleigh wave data were windowed using a time variable filter (Landisman et al., 1969), and the Fourier amplitude and phase calculated at each frequency of interest via a fast Fourier transform. The data were manually inspected to ensure a continuous dispersion curve, a SNR greater than 3 and peak energy between the approximate frequencies

of interest, 0.01 Hz to 0.07 Hz resulting in 1053 events and 47227 ray paths going into the final inversion.

2.3.2 1-D phase velocity inversion.

We determined the average dispersion curve for the area using a 1-D version of the two-plane wave inversion method (Forsyth et al., 2005). The inversion was completed in two steps, with the first stage utilising a simulated annealing method to fit the two plane wave parameters for each event, while trying a range of starting phase velocities for the model between 3.00-4.40 km/s (Press et al., 1992). This ensured a global starting model was found for input into the second stage which utilised an iterative damped least squares inversion (Tarantola et al., 1982) (Figure 3). The inversion simultaneously solves for the phase velocity, azimuthal anisotropy and wave parameters for each event. We do not calculate azimuthal anisotropy for the ambient noise as a systematic variation in phase with azimuth due to an inhomogeneous source distribution could easily be mapped into estimates of azimuthal anisotropy (Harmon et al., 2010; Yao & van der Hilst, 2009). We obtained an azimuthal anisotropy result for the teleseisms, but we do not interpret it as it is beyond the scope of this paper. There are some differences between the anisotropy model and that of Gallacher et al. (2016), which are due to the nodal spacing and additional data included in the inversion. For completeness we plot the anisotropy result in Supplementary Figure S10 and proceed focusing on the isotropic result. We assume an a priori error of the phase velocity model parameters (square root of the diagonals of Cmm) of 0.2 km/s (Supplementary figure S3) (Forsyth et al., 2005). The a priori error of the data (square root of the diagonals of Cnn, the data covariance matrix, eq. 1) are initially assigned as arbitrary value of 0.2, and as the data is normalized to a maximum value of 1 for each event, this yields a relatively conservative 20% error for the data. After the initial inversion the a priori error in the data for each event is defined by the misfit between the data for the event and the starting model of the previous iteration (Forsyth et al., 2005).

We set a minimum threshold for the a priori data covariance matrix of 0.03^2 or roughly 3% error of our normalized data, which are determined from the fits to the data as the inversion evolves. In other words we can fit 97% of the data to the normalized value of 1. Then we assign the average event misfit to the individual teleseismic data a priori error for a given teleseismic event and update at each step during the inversion. The reweighting of the data has an effect similar to using an L1-norm, by minimizing the effect of outliers or poorly fit data.

2.3.3 2-D phase velocity inversion.

We used the two plane wave method of Forsyth & Li (2005) at each period to invert for a phase velocity map using the amplitude and phase measurements described above from the teleseismic events, using 2-D finite frequency kernels (Yang & Forsyth 2006; Zhou et al., 2004). We used the same nodal parameterisation as used in the ambient noise tomography, i.e., a 0.25° x 0.25° nodal grid with the outermost row and column spaced at 1° to absorb velocity heterogeneities outside the target region (Figure 2). The average 1-D phase velocity described in the previous paragraph is used as our starting model at each period. The phase velocity inversion used 2-D finite frequency kernels (Forsyth et al., 2005; Nishida, 2011; Tromp et al., 2010; Yang et al., 2006) and an iterative damped least squares approach (Tarantola & Valette 1982) (eq. 1), which solves for phase velocities at each node, and the plane wave parameters for each event. We use the same Gaussian averaging scheme described above to generate higher resolution phase velocity grids at 0.1 x 0.1°. The phase velocity at the nodes represent an average phase over the smoothed area around the node, so the final phase velocity maps at 0.1 x 0.1° resolution are determined from the Gaussian distance weighted contributions of the nearest nodes to each pixel. For our a priori model covariance we use 0.2 km/s^2 for the inner nodes and 2 km/s^2 for the outer nodes used to absorb velocity heterogeneity outside the array along the diagonals of C_{mm}. We use the same

scheme described above for the 1-D teleseismic phase velocity estimate, to determine the values for the diagonals of the data covariance matrix described in section 2.3.2. We present the formal uncertainty from the last iteration of the inversion, which is propagated from the nodal parameterisation to the higher density grid using the Gaussian weights of each node at each pixel using the full covariance matrix. The inversion is run twice. After the first set of inversions, events with phase misfits of >4 s are removed from the starting dataset and this is the input used for the final set of inversions. The removal of these poorly fit events is necessary as it removes waveforms with complicated source radiation patterns and other effects not accounted for in the inversion.

2.4 Joint Inversion for Shear Velocities

For the shear velocity inversion, we inverted each pixel of the phase velocity maps across all periods for a 1-D shear velocity structure at every node as a function of depth (Figure 3). The combined 1-D shear velocities at every pixel collectively form the 3-D volume. We used the phase velocity maps from the ambient noise for 8–26 s and the phase velocity maps from the teleseismic results for 29–100 s. The transition at 26 s from one data-type to another is chosen based on the relative amounts of data, i.e. where the teleseismic has a greater number of ray paths. Where the ambient noise and teleseismic phase velocity maps overlap, they are within uncertainty of each other, e.g. at 20–33 s (Figure S2).

We used an iterative damped least squares inversion (Tarantola & Valette 1982) and parameterised the shear velocity every 5 km vertically with 0.1° x 0.1° pixel size for the upper 50 km. For deeper depths we use an irregular spacing increasing from 10–50 km spacings to match that of Gallacher et al. (2016). We further tested a regularly spaced 5 km model and found results within the uncertainties of our preferred model (Supplementary Figure S5). The partial derivatives that relate variations in shear velocity to changes in phase

velocity were calculated using DISPER80 (Saito, 1988). We assigned a nominal a priori standard error of 0.2 km/s for the shear velocity starting model and fixed the Vp/Vs ratio to 1.8, which is the crustal average from receiver function analyses (Hammond, et al., 2011; Stuart et al., 2006) and also a typical mantle value (Dziewonski & Anderson, 1981). Variations in the choice of Vp/Vs (1.5–2.1 the observed Vp/Vs ratios in this area) produced results within uncertainty and we present the formal uncertainty from the inversion in Figure 3. We show the improvement between the 1-D inversion and 2-D inversion in Supplementary Figure S6 and Table S1, and give the median values for the total phase time misfit, the RMS of the phase time misfit and RMS of the Real and Imaginary parts of the teleseismic inversions, and median and RMS of the phase misfit for the ambient noise inversion. Finally, we interpolated the velocity structure to 1 km depth for presentation purposes using a linear interpolation.

3.0 Uncertainties and resolution

To examine the resolution of the phase velocity tomography, we produced checkerboard resolution tests (Figure 4) and synthetic structure recovery tests (Figure 5). Checkerboard tests were produced at lateral length scales of 70 km (periods 8–40 s), and 165 km (~1.5°, periods 8–100 s)(See supplementary S7 and S8 for further checkerboard tests at length scales of 110 km (1°) and 220 km (2°)). We show the checkerboards at the shortest and longest periods for the ambient noise (8 and 26 s) and teleseisms (29 and 100 s). In the period range where the two data sources overlap, the teleseisms offer improved resolution at periods longer than 29s, without losing resolution for crustal structure provided by the ambient noise. We also mask results outside the 2σ standard error contour from the phase velocity inversion. This is the formal uncertainty of the inversion from the linearised iterative least squares at the last iteration. Errors are propagated to the higher density grid in a similar fashion to the phase velocities.

The checkerboard tests indicate that 70 km length scale anomalies are well recovered for 8–40 s period, and 165 km length scale anomalies are resolved for all periods within the 2σ error contour (Figure 4). Inside the rift, anomalies are resolved at 70 km length scales for 8–40 s period, and 110 km anomaly length scale anomalies can be resolved using periods of less than 71s (Figure S7). These periods are reflective of crustal and mantle depths which are discussed here down to ~120 km depth (Figure S7). Off-rift, 70 km length scale anomalies are well resolved at periods less than 17s for the ambient noise and at periods less than 40 s from the teleseisms. The 110 km length scales anomalies off-rift (Figure S7), can resolve anomalies at periods less than 71s. The 165 km length scale anomalies for all periods, both on and off-rift, are well resolved, however amplitude decreases at the longer periods. For checker anomaly length scales of 220 km, features are resolved at periods up to 100s (Figure S8). The decrease in amplitude recovery is likely related to the broad sensitivity kernels for the longest periods (first Fresnel zone ~500-1000 km wide for 100s period (Yoshizawa & Kennett, 2002)) and fewer ray paths. For our model, based on the recovery tests, it is apparent that we are likely underestimating the amplitude of the velocity anomalies at asthenospheric depths. This is particularly noticeable beneath the Ethiopian Plateau deeper than 50 km depth where the wave speed variations at mantle depths are likely stronger than what is shown here. In areas where ray coverage is sparse we have poorer resolution, such as the Red Sea, Gulf of Aden and eastern part of Afar. There is also northeast-southwest smearing of the checkerboards beneath the Red Sea Rift and northwest-southeast smearing beneath Yemen. Consequently, we do not interpret these areas.

To test whether the presence of water or variations in sediment thickness were biasing our model, we performed tests with a 3 and 5 km thick water layer in the Red Sea and Gulf of Aden and with a sediment layer in the rifts using velocity and density values from CRUST1.0

(Laske et al., 2013). The tests produced shear velocity models within uncertainty of the model we show in this paper, and the layers are within the upper 5 km, which we do not resolve.

In the synthetic recovery tests, we input a slow velocity anomaly of similar magnitude to our output models in the MER and beneath the Ethiopian Plateau. Broadly, based on depth sensitivity kernels (Figure 3), features >70 km in length scale are well resolved in the upper 70 km and features >150 km in length are resolvable at all depths of the shear velocity model. We show periods at the minimum and maximum period for the ANT (8 and 26s) and teleseisms (29 and 100s) to show the full range of recovery (Figure 5). Within the rift, the recovery tests indicate phase velocity variations are resolved in our models at all periods for a continuous rift and for segmented anomalies (Figure 5 and S9), though at periods >71 s the anomaly beneath the rift is less elongate and focusses to the northwest of the MER. Off-rift synthetic recovery tests at periods <29s, indicate the two slow velocity features are resolvable if they are >70 km wide. At longer periods the two anomalies are no longer distinct. Synthetic recovery tests within the Red Sea and Gulf of Aden Rifts suggest there is smearing in a northeast direction particularly for the Gulf of Aden at longer periods which may interact with the onshore rift in Djibouti and northeast Afar.

To examine vertical resolution, we perform a spike test (Backus & Gilbert, 1970) for a range of model depths (Figure 6). These kernels show the recovery of a spike function based on the diagonals of the formal resolution matrix. The formal resolution matrix is derived from the damped least squares inversion where Resolution: $\boldsymbol{R} = \left(\boldsymbol{G}^T \boldsymbol{C_{nn}}^{-1} \boldsymbol{G} + \boldsymbol{C_{mm}}\right)^{-1} (\boldsymbol{G}^T \boldsymbol{C_{nn}^{-1}} \boldsymbol{G})$. $\boldsymbol{G}$ is the matrix of partial derivatives from the kernel at each node, $\boldsymbol{C_{nn}}$ is the data covariance matrix and $\boldsymbol{C_{mm}}$ is the model covariance matrix (Saito, 1988). Resolution ranges between 0-1, where 1 indicates a completely resolved model parameter (e.g. velocity of a layer) and 0

means not resolved. The kernels suggest shear velocities are resolvable down to 150 km depth (Figure 3 and Figure 6) after which the resolution starts to deviate from the typical bell curve shape. At the shallowest depths (7-22 km), depth slices averaged over ±10 km are resolved, whereas the deepest slices at 142-162 km depth also include sensitivity to a broader depth range between approximately 100 and 250 km depth.

4.0 Results

4.1 1-D dispersion curves and shear velocity model

Average 1-D dispersion curves measured from the ambient noise and teleseismic data are shown in Figure 3. Phase velocities range from 2.93 ± 0.02 km/s at 8s to 3.87 ± 0.03 km/s at 100s (Figure 3 and Figure 7). Where the phase velocities from the ambient noise and teleseisms overlap (20-33 s) (Figure S2), the velocities are similar to one another and within the standard error. The shear velocity structure is displayed in Figure 3b with shear velocities ranging from 3.10 ± 0.02 km/s at 5 km depth to 4.42 ± 0.03 km/s at 150 km depth. The average 1-D shear velocities are slower than the input model (green line) at most depths except from 40-80 km depth. In Figure 3c we present the sensitivity kernels, which indicate the depths of peak sensitivity for the shear velocity inversion at 8, 15, 20, 26, 29, 40, 71 and 100 s period. The kernels suggest 150 km depth is the limit of our sensitivity.

4.2 2-D Phase Velocities

We generate phase velocity maps from 8-100 s (Figure 7 and Figure S10) and observe velocity variations that correlate with geologic and tectonic features. Phase velocities are more variable at shorter periods ranging from 2.85-3.45 ±0.04 km/s at 10 s becoming less laterally variable at 100 s period (3.80-3.90 ±0.06 km/s), though amplitude recovery reduces with increasing period as discussed above.

Within the rift system, the MER is the slowest region of our study for all periods (at 10s the Red Sea is slower but due to ray path bias, we do not interpret this region). We observe minimum velocities ranging from 2.90 ±0.03 km/s at 10 s to 3.82 ±0.04 km/s at 100 s period. Beneath Afar, velocities are ~0.20 km/s faster than the MER at all periods. Phase velocity ranges from 3.15 ±0.03 km/s at 10 s to 3.90 ±0.04 km/s at 100 s period. Within the rifts we observe slow velocity anomalies that vary in strength, size and location at <71 s. For instance, at 26 and 29 s periods the anomalies have a punctuated character, and a size of ~100 km.

The velocity structure on the Ethiopian Plateau is variable, exhibiting both fast and slow velocity regions across the period range of interest. The eastern part of the Ethiopian Plateau is slow at short periods (from 8 to 26 s) with velocities of 3.00 ±0.04 km/s at 10 s to 3.50 ±0.05 km/s at 26 s period. At 20 to 26 s period, the shape of the two slow velocity regions connect which may in part be due to smearing according to our resolution tests (Figure 5). At longer periods (>29 s period), phase velocities beneath the eastern part of the Ethiopian Plateau are similar to background phase velocity values (~3.80-3.90 ±0.05 km/s). In contrast, the western part of the Ethiopian Plateau is the fastest area of our study at all periods with phase velocities of 3.35 ±0.04 km/s at 10 s period increasing to 3.92 ±0.05 km/s at 100 s depth.

In the phase velocity maps the slowest anomalies are typically beneath the MER (Figure 7), whereas this is only true at <40 km and >150 km depth in the shear velocity maps (Figure 8). This likely reflects the broad depth sensitivity of phase velocity measurements and the large contrast in crustal thickness and velocity between Afar and the MER. In other words, the

slow thick crust with a slow velocity mantle in the MER generates slow velocities at all periods in the phase velocity maps. In Afar, thin crust with faster but anomalously slow mantle beneath yields relatively high phase velocities at short periods (8–20 s) and lower velocities at longer periods (50–100 s) when the sensitivities are averaging more mantle than crust.

4.3 3-D Shear Velocity Structure

At lithospheric depths (10-80 km), we observe strong lateral variations in shear velocity, up to 0.85 km/s across our study region, which likely reflect a combination of significant changes in crustal thickness and variability in mantle structure. Figure 8 and Figure 9 show depth slices and cross-sections through the shear velocity model, respectively. The slowest velocities in the region are beneath the MER from 10–50 km depth and the Danakil depression from 50-80 km depth (due to variations in lithospheric thickness). For instance, at crustal depths (10 km) we find Vs = 3.00 ±0.03 km/s, and at mantle depths (60 km) we find Vs = 4.05 ±0.03 km/s (Figure 8 a-c). In profile A–A' (Figure 9a) south of the MER, there is a fast lid visible between 37–38.5° E at 60–80 km depth. Within the rift, this fast lid is broken by slow velocity anomalies before becoming prevalent again near the Arabian Peninsula.

At 20-40 km depth there is a slow velocity region centred ~100 km southeast of Lake Tana beneath the eastern part of the Ethiopian Plateau (3.10-3.85 ±0.04 km/s at depths of 10 to 40 km respectively), and another anomaly ~100 km east of this anomaly centred beneath the border fault region. These anomalies are not present below 60 km depth (Figure 8c).

The western Ethiopian Plateau is one of the fastest regions at 20-40 km depths with velocities >3.80 km/s at 20 km and >4.15 km/s at 40 km (±0.04 km/s), but is close to the average velocity across the region at 60 km. Profile B-B' (Figure 9b) shows there is a high velocity

lid (velocity >4.15 km/s), from 60-80 km depth west of the rift (<38.5° E), and to the east of the rift (>40° E).

Afar has some of the fastest velocities in the region at 20 km depth (~3.80 km/s), which likely reflects the thinner crust in this region compared to the Plateau. At 40-60 km depth, the Afar region is characterised by several punctuated slow velocity regions with velocities <3.9 km/s, which are coincident with regions of active hydrothermal sites (stars in Figure 8) or recent volcanism (red polygons in Figure 8). Specifically, beneath the crustal magmatic segments and along the TGD (shown in Figure 1 as red polygons and dashed line respectively) the velocities are ~0.2 km/s slower than the rest of Afar at all lithospheric depths.

At asthenospheric depths (>60 km in Afar and >80 km in the MER and Plateau), we also observe several punctuated slow velocity regions. Specifically, in the 80-120 km depth range, the region beneath the MER is the slowest in the region with velocities <4.15 km/s (Figure 8 and S11). The slow velocity anomaly is not centred beneath the rift but is offset towards the west, beneath Addis Ababa and straddling the rift. There are two other slow velocity regions with velocities <4.15 km/s located near the Red Sea and the Gulf of Aden. Within Afar, in this depth range, the slow velocities are not as strong.

The slow velocity anomalies within the rift appear to systematically extend to shallower depths going from the MER northwards. Profile A-A', along the MER rift axis (Figure 9a), extending into Afar, shows the relationship between the slow velocity anomalies. Near the MER, the slow velocities are visible beneath the fast lid, extending from 80-120 km depth using the 4.05 km/s contour (Figure 9a). Going northwards, the slow velocity anomalies are centred at shallower depths going to 75 km and then to 65 km depth beneath Afar. Although the progression is intriguing, given our depth resolution, the shallowing itself is not particularly well-resolved. The base of the anomalies appears fairly constant at ~120 km

depth. There does not appear to be much variation in structure at greater depths in our models though this is close to the limits of our depth resolution.

The strongest anomalies at crustal depths within the MER and the Ethiopian Plateau, are displaced from the strongest anomalies in the asthenosphere, while in Afar the anomalies in the asthenosphere are close to regions of geologically recent volcanism. In the MER the slow velocities at 20 km depth are located ~100 km southwest of the slowest velocities in the asthenosphere. Beneath the Ethiopian Plateau, velocities at asthenospheric depths are faster than those within the MER and the slowest asthenospheric velocities that may link to those within the crust off-rift, are again located within the asthenosphere beneath the MER.

5.0 Interpretation

Our results provide an absolute seismic velocity model for the crust and upper mantle beneath the rift and the Ethiopian Plateau. One primary new component of our model is the higher resolution crustal and upper mantle structure beneath the Ethiopian Plateau. In addition, the broader period range used here to invert for shear velocity structure also improves estimates of the crust and upper mantle structure across the entire region in comparison to previous work. The new absolute shear velocity structure allows us to examine the relationship between the lithosphere-asthenosphere system off-rift beneath the Ethiopian Plateau and Somalian Plateau relative to the active tectonic and mantle dynamics within the rift. Much of the shallow structure (< 40 km depth) is consistent with the ambient noise tomography of Chambers et al. (2019) in the regions of overlap. Therefore, we briefly discuss crustal structure and implications, before focusing on the new results including: 1) off-rift structure beneath the Ethiopian Plateau and 2) mantle structure for the entire region, which has improved resolution over previous studies, owing to our broader period range and joint inversion approach.

5.1 Crustal Structure

At shallow depths (10-40 km) we observe the largest range in shear velocity beneath the rift. This is likely owing to changes in crustal thickness, melt and temperature (Bastow et al., 2010; Chambers et al., 2019; Dugda et al., 2007; Hammond, 2014; Kim et al., 2012; Korostelev et al., 2015). Faster velocities (3.8–4.10 ±0.04 km/s) beneath Afar at 10-40 km depth are consistent with the presence of the mantle in this depth range in the region and consistent with a thinner crust (16–25 km thick crust (Hammond et al., 2011)) in comparison to surrounding regions, for instance slower velocities (3.00–3.80 ±0.03 km/s) beneath the MER and (3.10-3.85 ±0.04 km/s) beneath the Ethiopian Plateau, while crustal thicknesses are 25-35 km and 35–40 km thick for the MER and Ethiopian Plateau, respectively (Cornwell et al., 2010; Dugda et al., 2005; Ogden et al., 2019; Stuart et al., 2006). The slower crustal velocities within the MER are likely a result of higher temperatures and/or the presence of partial melt in the crust, which is similar to interpretations by previous studies which observe slow crustal velocities (e.g. Bastow et al., 2010; Chambers et al., 2019; Hammond et al., 2014) and high conductivities (Hübert et al., 2018; Whaler & Hautot 2006). If we assume the slower velocities in the MER are solely from melt we can relate the velocity reduction to melt using the experimental relationship of 0.1 km/s decrease in shear velocity requires 1% melt (Caricchi et al., 2008). Comparing the velocity reduction in the slowest region of the MER with respect to the western Ethiopian Plateau, we require 3.0% partial melt which is within the range interpreted in previous teleseismic tomography studies (0.6–4.0% partial melt) (Bastow et al., 2011; Civiero et al., 2015; Ferguson et al., 2013; Gallacher et al., 2016) and surface wave tomography (1.1-2.0%) (Chambers et al., 2019). It should be noted that while velocities are affected by volume of melt, the shape and aspect ratio of melt inclusions likely have a larger influence on velocity (Blackman & Kendall, 1997; Hammond & Kendall, 2016), thus the 4.0% estimate from previous studies is an upper bound on melt fraction.

Where slow velocities are observed beneath crustal magmatic segments in our model (>0.2 km/s slower than surroundings, Vs = 3.50 ±0.02 km/s), magmatic emplacement is also likely. A similar interpretation has been made for the origin of the slow velocities in a surface wave derived model and geochemical analysis (e.g. Chambers et al., 2019; Rooney, 2020b) (Figure 8). Seismicity studies find evidence for lower crustal earthquakes in the rift in areas where temperatures should be too high for brittle failure and suggest lower crustal earthquakes are generated by fluid/magmatic injection from the mantle (La Rosa et al., 2021; Muluneh et al., 2021). Furthermore, studies find higher Vp values at lower crustal depths (6.8–7.2 km/s) (e.g. Daly et al., 2008; Keranen et al., 2004; Mackenzie et al., 2005), which when coupled with high Vp/Vs ratios (1.8–2.1) (Daly et al., 2008; Hammond et al., 2011) and high conductivities (resistivity 0.8 log(**Ω**m)) (Whaler et al., 2006) suggest the lower crust is undergoing significant modification by active magmatic intrusions (e.g. Hammond et al., 2010; Keir et al., 2009; Kim et al., 2012). These results are also supported by anisotropy which requires partial melt stored in dykes and sills throughout the crust (Bastow et al., 2010; Chambers et al., 2021; Hammond, 2014; Keir et al., 2011).

At the westernmost part of the Ethiopian Plateau, located 250-500 km from the rift, we can obtain information about the pre-rift structure. The distance from the rift, coupled with geological studies which find little evidence for eruptions (e.g. Jones, (1976); Rooney, (2019)), suggests the westernmost part of the Ethiopian Plateau (Figure 1) has been minimally impacted by rifting and hotspot tectonism (Jones, 1976; Rooney, 2019). We interpret the crustal velocity observations as being most similar to original plate structure before rifting. We choose this region as it is significantly further from the rift than the Somalian Plateau that we have imaged. While previous geological studies commonly regard the Somalian Plateau as having been little modified by flood basalt volcanism, the spatial

extent of geophysical studies are limited for this region and are located close to the rift. Ogden et al., (2019), performed receiver function analysis in the same area, finding crustal thicknesses of ~30 km at the western edge of the Ethiopian Plateau and interpreted the area as being unaffected by lower crustal intrusion from the Oligocene flood basalts or younger rifting, consistent with our observations.

The slow velocities observed within the Ethiopian Plateau, southeast of Lake Tana suggest there may been relatively recent magmatic intrusion into the crust. The slow velocity regions are all shallower than 40 km with similar magnitudes to the slow velocities observed in the MER, with little evidence for slow velocities at greater depth. The locations of the slow velocity anomalies broadly correspond to the locations of known geothermal activity and past volcanism (Figure 8). The last major volcanic event on the Ethiopian Plateau was >21 Myrs (Rooney, 2017) though there is evidence for limited Quaternary activity along the YTVL and southwest of lake Tana (Kieffer et al., 2004; Meshesha & Shinjo, 2007). Simple conductive cooling calculations for the 1-D thermal heat equation indicate that a 1300°C thermal anomaly would dissipate in <10 Myr (Figure S12 and Text S1). Therefore, it is unlikely that a remnant thermal anomaly could explain our observations, and we suggest there has been further recent magmatic emplacement. Our recovery tests at > 15 s period (Figure 5), suggest there may be some smearing between the anomalies in the region, so we cannot differentiate whether there are multiple isolated magma bodies or a broader region of melt. In addition, although there does not appear to be a slow velocity region at > 40 km depth, our lateral resolution may prevent us from imaging a small conduit for melt at these depths or if the slow velocity anomaly is an isolated and shallow magma body with no feeder system.

5.2 Lithospheric Mantle Structure

In the upper mantle we require a fast lid in the average 1-D shear velocity model for the region (Figure 3), and we also observe a fast lid in many parts of our 3-D shear velocity

model. In the average 1-D shear velocity model, the maximum fast lid velocity is slower than those observed in other continental settings and global averages (maximum of 4.30 ±0.05 km/s for our model in comparison to 4.45 km/s for ak135) (Kennett et al., 1995). In the 3-D model, the fast lid thickness/presence is variable. Off-rift the fast lid extends to 60–80 km depth but is absent beneath Afar. The velocities just beneath the crust also vary depending on tectonic region suggesting there is a lateral variation in temperature, composition, and/or melt content. For instance, the MER at 50–60 km depth is characterised by velocities that are ~0.1 km/s slower relative to the western Ethiopian Plateau. The slower velocities in the MER are likely caused by hotter temperatures and/or melt caused by upwelling in the rift.

The fast lid is intermittently present in our model. The fast lid is most prominent off-rift beneath the rift flanks and Ethiopian Plateau in Profile B-B' (Figure 9b), in regions less affected by rifting. In the rift Profile A-A' which extends from the southern MER to the Arabian Peninsula (Figure 9a), a weaker fast velocity zone (Vs = 4.1-4.15 km/s) is intermittently visible within the rift and is underlain by the slowest asthenospheric velocities (discussed in the next section). The fast lid becomes prevalent again near the Arabian Peninsula. The base of the fast lid is commonly associated with the LAB (Fishwick, 2010; Lavayssière et al., 2018; Rychert et al., 2012, 2005), and we therefore plot the S-to-P LAB results of Lavayssière et al. (2018) on our cross-sections (Figure 9 red diamonds in lower panels). Overall, we find good agreement between the locations of our fastest velocities (Vs >4.15 km/s) and the existence of a strong LAB phase from the S-to-P results. This suggests that the S-to-P result is detecting a strong, sharp velocity drop at the base of the fast lid where it exists. Our result, with no discernible fast lid in Afar, is consistent with S-to-P results which also did not find a strong, significant LAB phase beneath the majority of the rift (Lavayssière et al., 2018; Rychert et al., 2012). In summary, a fast velocity lid is required to achieve a negative LAB velocity gradient that is imageable by S-to-P. Since, S-to-P imaging

requires strong, sharp velocity gradients it also implies that the velocity drop at the base of the lid in our model may be sharper than that in our smooth model, although our resolution precludes further investigation. The presence of the slowest asthenospheric velocities (3.98-4.06 ±0.03 km/s) beneath areas where receiver functions do not detect a significant LAB phase (Lavayssière et al., 2018; Rychert et al., 2012), is consistent with a lack of fast lid caused by a melt-infiltrated lithosphere (Bastow et al., 2010; Kendall et al., 2006, 2005; Lavayssière et al., 2018). We note that we do not see strong evidence for a lithospheric drip beneath the Ethiopian Plateau as hypothesized based on geochemical analyses, although we cannot exclude the possibility that it has descended deeper into the mantle outside of our resolution (e.g. Furman et al., 2016).

5.3 Asthenospheric Anomalies

At asthenospheric depths, >80 km beneath the Ethiopian Plateau we observe velocities of 4.20 ±0.05 km/s which by itself does not necessarily require the presence of partial melt. The asthenospheric velocity is lower than the global average at that depth (4.45 km/s) using ak135 (Kennett et al., 1995), but is consistent with a previous surface wave derived shear velocity model in the region which also observed mantle velocities of ~4.20 km/s (Gallacher et al., 2016) (Figure 3b and Figure 8). The velocity can be explained by a thermal anomaly of 100–170°C (e.g. Gallacher et al., 2016), which is consistent with petrological constraints of the regional mantle potential temperature (Armitage et al., 2015; Ferguson et al., 2013; Rooney et al., 2012b). However, receiver functions image a strong, sharp discontinuity beneath the Ethiopian Plateau (Lavayssière et al., 2018; Rychert et al., 2012), and these studies as well as many others, have shown that another factor besides elevated temperatures is required to explain strong sharp velocity drops with depth. Partial melt is the most straightforward explanation for a host of similar observations globally (e.g. Harmon et al., 2021; Rychert et al., 2020). Therefore, if melt does exist in the asthenosphere beneath the Ethiopian Plateau, it

must be in a more limited depth and/or lateral area than resolvable by surface waves in this region.

Within the rift we observe punctuated slow velocity anomalies (Vs <4.05 km/s) at asthenospheric depths of > 60 km, which are ~110x80 km wide, spaced ~70 km apart, and have a base at ~120 km depth Figure 9a. The deep punctuated slow velocity anomalies that we observe are similar in scale and position to features imaged in a number of previous tomographic studies (Bastow et al., 2008, 2005; Gallacher et al., 2016; Hammond et al., 2013). However, they do not correspond spatially with the crustal magmatic segments at the surface. The northernmost anomaly with the shallowest starting depth (60 km) exists beneath Afar, the region in the latest stage of rifting (9% velocity decrease when comparing to the rift flanks), while for the MER the shallowest starting depth for the slow velocity bodies is at ~80 km depth. We note that absolute depths could vary by 20-30 km given our sensitivity at asthenospheric depths, although the trend is compelling. Mantle potential temperatures in the rift are only moderately elevated, ~1450°C (Ferguson et al., 2013; Petersen et al., 2015; Rooney, Herzberg, et al., 2012) based on models of volcanic rock geochemistry. With this temperature, we would expect velocities to be reduced by ~3% using a Burgers model (Jackson & Faul, 2010) for a peridotite mantle and an estimated geotherm for the MER (Chambers et al., 2019). Composition and temperature are therefore not sufficient to account for the velocity reduction, which suggests a fluid component is required in the asthenosphere beneath the rift. We postulate the fluid component is most likely partial melt, from the abundance of Quaternary volcanism at the surface, which is in agreement with previous tomographic studies (Bastow et al., 2008; Chambers et al., 2019; Gallacher et al., 2016). This is further supported by anisotropy studies which require melt as inclusions along the rifts (Bastow et al., 2010; Chambers et al., 2021; Hammond, 2014; Hammond et al., 2010; Keir et

al., 2005; Kendall et al., 2006). The anomalies occur at depths consistent with previous geochemical estimates of melt generation (53–120 km depth) (Ferguson et al., 2013; Rooney et al., 2005).

The punctuated slow velocities in the asthenosphere (Figure 9a), are present beneath younger areas of the rift where the crust and lithosphere is not significantly thinner than beneath the Ethiopian Plateau (40 km thick crust and 80 km thick lithosphere (Lavayssière et al., 2018; Stuart et al., 2006)). Furthermore the anomalies persist into areas of later stage rifting in the northern section of A-A' in Afar (Figure 9a) where the crust is thinner (crustal thicknesses of 22 km (Hammond, et al., 2011)). These observations suggests punctuated melt supply starts prior to significant crustal and plate thinning.

Punctuated slow velocity anomalies beneath rifts are not isolated to this study and have been observed beneath the EAR (Bastow et al., 2008; Civiero et al., 2015, 2019; Gallacher et al., 2016; Hammond et al., 2013) and more mature rifts and mid-ocean ridges, e.g. Gulf of California, Red Sea Rift, the Mid Atlantic Ridge (Harmon et al., 2020; Lekic et al., 2011; Ligi et al., 2012; Wang et al., 2009). The processes generating separated slow velocity anomalies beneath the EAR are debated (e.g. Bastow et al., 2008; Civiero et al., 2015; Gallacher et al., 2016; Ligi et al., 2012). The main hypotheses for the slow anomalies are decompression melting focused by buoyancy driven upwelling from the release of melt (Gallacher et al., 2016) or decompression melting focused by non symmetrical mechanical thinning of the lithosphere (Bastow et al., 2008, 2005) and steep lithosphere asthenosphere boundary gradients that developed during early-stage rifting (Holtzman & Kendall, 2010; Kendall et al., 2005). Other hypotheses are the presence of smaller diapiric upwellings (Hammond et al., 2013) and mantle plumelets (e.g. Civiero et al., 2019). The spatial position of our anomalies which are broadly within the rift coupled with larger, slower velocity anomalies, the tops of which shallow towards more advanced stages of rifting, favours rift

related upwelling and we do not observe a connection to multiple plumelets from deeper depths. However, within the central MER the punctuated slow velocity anomalies are offset to the northwest of the rift axis, beneath the rift flanks in agreement with previous body wave tomography (Bastow et al., 2008, 2005). The offset in the anomalies suggests that pre-existing structures and topography of the LAB may also have a control on melt migration. Anisotropy in the MER is strongest near the rift flanks and studies have suggested strong azimuthal anisotropy coupled with velocities slow enough to contain melt reflect regions of steepest LAB gradient (Bastow et al., 2008, 2005; Holtzman et al., 2010; Kendall et al., 2006). One possibility is that the punctuated slow velocity zones are in part controlled by variations in LAB topography in the earlier stages of rifting, where the rift is narrow, but their shallowing and more central position at more advanced rifting suggest the current locus of extension is the primary control.

Within the MER the slowest crustal velocity anomalies at 10–40 km depth are not located directly above the slowest velocity anomalies at asthenospheric depths (> 80 km) (Figure 9). As previously discussed, the anomalies at both depths are slow enough to require the presence of partial melt. One possible explanation is that melt migrates laterally to the crustal anomalies, potentially guided by a permeability boundary at the base of the plate that thins towards the rift, focusing the melt there (Sparks & Parmentier, 1991). Lateral melt migration has also been proposed by previous studies in the region (Bastow et al., 2005; Gallacher et al., 2016; Holtzman and Kendall 2010; Kendall et al., 2005).

Off-rift, beneath the Ethiopian Plateau, slow crustal velocities (located at ~38° E, 11° N and ~39.5° E, 11° N Figure 8 and 9) are also not located above the slowest asthenospheric velocities which are located beneath the rift. This situation is harder to reconcile via lateral melt migration unless there are pre-existing lithospheric cracks (Sandwell & Fialko, 2004) from the rift to beneath the Ethiopian Plateau. Overall, lateral melt migration is unlikely

given that neither our result nor that from receiver functions supports lithospheric thinning toward the off rift slower crustal velocities (Lavayssière et al., 2018). Another possibility is that melt is ephemeral. In other words, melt was once present in the asthenosphere beneath the slow crustal anomalies of the plateau but it has now drained to the crust and/or frozen into the mantle. This idea is based on geodyanmic modeling work that shows that melt need not necessarily immediately leave the mantle via a vertical ascent path (Hebert & Montési, 2010; Sim et al., 2020; Sparks & Parmentier 1991). For instance, recent geodynamic modelling of two-phase flow shows that for spreading rates similar to those of the MER, melt is predicted to rise and accumulate beneath a permeability boundary at the base of the plate (Sim et al., 2020). The melt eventually freezes into the base of the plate and/or moves along the base of the permeability barrier towards the surface, essentially draining the mantle of melt before eventually being replenished by upwellings from below. Both the episodic nature of the melt supply and the fact that some melt is predicted to freeze into the plate mean that the amount of melt imaged in the asthenosphere at any given time need not synchronously balance the amount of melt in the crust and/or at the surface of the Earth. Of course, this modelling work has not yet evolved to incorporate the variations in lithospheric and crustal thicknesses that occur in a continental rift. However, such work offers strong evidence of such a possibility in rift systems. Ephemeral melt has also been invoked to explain punctuated anomalies and variable presence of channelised melt beneath the oceanic lithosphere (Carbotte et al., 2021; Harmon et al., 2020, 2021; Rychert et al., 2021, 2020; Wang et al., 2020). It presumes that melt generation is episodic and that melt migration is faster than generation so that the mantle is effectively drained. A third possibility is that melt is present in the asthenosphere beneath the slow crustal velocity anomalies of the plateau (Civiero et al., 2015; Keranen et al., 2009), but is localised in pockets that are below our resolving power. This possibility is supported by our resolution tests that show that amplitude recovery beneath the plateau is muted, and

therefore velocities could be slower than those of our model (Figure 5). It is also supported by receiver function imaging of strong sharp velcoity drops beneath the plateau, which are most easily explained by a small amount of melt in the asthenosphere (Figure 9) (Lavayssière et al., 2018; Rychert et al., 2012). It should be noted that there is ongoing extension below the Ethiopian Plateau (Birhanu et al., 2016), which has been attributed to high gravitational potential energy or intrusive magmatism away from rift. While the areas of greatest extension are not in exactly the same location as the slow off-rift crustal velocities, it provides a mechanism to facilitate off rift crustal intrusion, and a mechanism to generate melt beneath it. Overall, our result suggests melt generation and migration may be dynamic processes, which require further study to fully understand rifting processes and the factors that dictate the locations of active volcanic/hydrothermal regions.

6.0 Conclusions

We present the results from a joint inversion of ambient noise and teleseismic Rayleigh waves to produce a 3-D absolute shear velocity map from 10-150 km depth, for the northern East African Rift. At crustal depths we observe significant lateral velocity variations which can partly be explained by variations in crustal thickness; velocities are slowest beneath the Main Ethiopian Rift and the eastern part of the Ethiopian Plateau, and are slow enough to require a component of partial melt. At 60–80 km depth a fast lid, consistent with previous measurements for the lithosphere-asthenosphere-boundary, is observed off-rift (>0.1 km/s faster than surroundings) and at asthenospheric depths beneath the Ethiopian Plateau we observe velocities only slightly slower (4.30 ±0.05 km/s) than global models. This slower velocity anomaly can be explained by elevated temperatures, although we cannot rule out the possibility of melt in smaller pockets beneath our area of resolution. Within the rift, velocities are significantly slower than off-rift and the fast lid is obscured where it is underlain by

asthenospheric punctuated slow velocity anomalies at 60-120 km depth. The asthenospheric slow velocity anomalies are interpreted as areas of partial melt which are infiltrating the lithosphere, and suggest punctuated melt supply starts prior to significant crustal and plate thinning. Furthermore, asthenospheric anomalies are not directly beneath the melt-rich crustal regions, including those off-rift, suggesting melt generation and migration are dynamic processes and/or that melt may migrate laterally within the mantle.

Acknowledgments

E.L.C acknowledges funding from NERC studentship NE/L002531/1. C.A.R. and N.H. acknowledge funding from NERC grants NE/M003507/1 and ERC grant GA 638665. D.K. is supported by NERC grant NE/L013932 and by MiUR through PRIN grant 2017P9AT72. We thank SEIS-UK (supported by NERC under agreement R8/H10/64.F) for use of instruments and computing facilities. Some figures were made using GMT (Wessel et al. 2013).

Data Availability Statement

All data used to generate the models are freely available from the IRIS Data Management Center (IRISDMC; https://service.iris.edu/fdsnws/dataselect/1/) funded through SAGE Proposal of the NSF under Cooperative Agreement EAR-126168. The networks used are:
RiftVolc Y6 (https://doi.org/10.7914/SN/Y6_2016), ARGOS XM (https://doi.org/10.7914/SN/XM_2012), Plateau YY (https://doi.org/10.7914/SN/YY_2013), EKBSE XI (https://doi.org/10.7914/SN/XI_2000), YOCMAL XW(https://doi.org/10.7914/SN/XW_2009), EAGLE geophysical XJ (https://www.fdsn.org/networks/detail/XJ_2002/), EAGLE geoscientific YJ (https://www.fdsn.org/networks/detail/YJ_2001/), Boina YZ (https://www.fdsn.org/networks/detail/YZ_2005/), AFAR07 ZE (https://doi.org/10.7914/SN/ZE_2007), Afar depression ZK (https://doi.org/10.7914/SN/ZK_2009), Africa Array AF (https://doi.org/10.7914/SN/AF), IU (https://doi.org/10.7914/SN/IU), GEOFON GE

(https://doi.org/10.14470/TR560404), Eritrea YR/5H (https://doi.org/10.7914/SN/5H_2011), Danakil depression ZR/2H (https://doi.org/10.7914/SN/2H_2009), GEOSCOPE G (https://doi.org/10.18715/GEOSCOPE.G).

Our final shear velocity model is available at https://doi.org/10.5258/SOTON/D1408.

References

Aki, K. (1957). Space and time spectra of stationary stochastic waves, with special reference to microtremors. *Bulletin of the Earthquake Research Institute*. https://doi.org/http://hdl.handle.net/2261/11892

Armitage, J. J., Ferguson, D. J., Goes, S., Hammond, J. O. S., Calais, E., Rychert, C. A., & Harmon, N. (2015). Upper mantle temperature and the onset of extension and break-up in Afar, Africa. *Earth and Planetary Science Letters*, *418*, 78–90. https://doi.org/10.1016/j.epsl.2015.02.039

Backus, G. E., & Gilbert, F. (1970). Uniqueness in the inversion of inaccurate gross Earth data. *Philosophical Transactions of the Royal Society of London. Series A, Mathematical and Physical Sciences*, *266*, 123–192.

Bastow, I. D. (2012). Relative arrival-time upper-mantle tomography and the elusive background mean. *Geophysical Journal International*, *190*(2), 1271–1278. https://doi.org/10.1111/j.1365-246X.2012.05559.x

Bastow, I. D., Keir, D., & Daly, E. (2011). The Ethiopia Afar Geoscientific Lithospheric Experiment (EAGLE): Probing the transition from continental rifting to incipient seafloor spreading. *The Geological Society of America Special Papers*, *478*, 51–76. https://doi.org/10.1130/2011.2478(04)

Bastow, I. D., Nyblade, A. A., Stuart, G. W., Rooney, T. O., & Benoit, M. H. (2008). Upper

mantle seismic structure beneath the Ethiopian hot spot: Rifting at the edge of the African low-velocity anomaly. *Geochemistry, Geophysics, Geosystems*, *9*(12). https://doi.org/10.1029/2008GC002107

Bastow, I. D., Pilidou, S., Kendall, J.-M., & Stuart, G. W. (2010). Melt-induced seismic anisotropy and magma assisted rifting in Ethiopia: Evidence from surface waves. *Geochemistry, Geophysics, Geosystems*, *11*(6), 1–19. https://doi.org/10.1029/2010GC003036

Bastow, I. D., Stuart, G. W., Kendall, J.-M., & Ebinger, C. J. (2005). Upper-mantle seismic structure in a region of incipient continental breakup: Northern Ethiopian rift. *Geophysical Journal International*, *162*(2), 479–493. https://doi.org/10.1111/j.1365-246X.2005.02666.x

Benoit, M. H., Nyblade, A. A., & VanDecar, J. C. (2006). Upper mantle P-wave speed variations beneath Ethiopia and the origin of the Afar hotspot. *Geology*, *34*(5), 329–332. https://doi.org/10.1130/G22281.1

Bensen, G. D., Ritzwoller, M. H., Barmin, M. P., Levshin, A. L., Lin, F.-C., Moschetti, M. P., … Yang, Y. (2007). Processing seismic ambient noise data to obtain reliable broad-band surface wave dispersion measurements. *Geophysical Journal International*, *169*(3), 1239–1260. https://doi.org/10.1111/j.1365-246X.2007.03374.x

Birhanu, Y., Bendick, R., Fisseha, S., Lewi, E., Floyd, M., King, R., & Reilinger, R. (2016). GPS constraints on broad scale extension in the Ethiopian Highlands and Main Ethiopian Rift. *Geophysical Research Letters*, *43*(13), 6844–6851. https://doi.org/10.1002/2016GL069890

Blackman, D. K., & Kendall, J.-M. (1997). Sensitivity of teleseismic body waves to mineral texture and melt in the mantle beneath a mid-ocean ridge. *Philosophical Transactions of the Royal Society A: Mathematical, Physical and Engineering Sciences*, *355*(1723),

217–231. https://doi.org/10.1098/rsta.1997.0007

Bosworth, W., Huchon, P., & McClay, K. (2005). The Red Sea and Gulf of Aden Basins. *Journal of African Earth Sciences*, *43*(1–3), 334–378. https://doi.org/10.1016/j.jafrearsci.2005.07.020

Boyce, A., Bastow, I. D., Cottaar, S., Kounoudis, R., Guilloud De Courbeville, J., Caunt, E., & Desai, S. (2021). AFRP20: New P-Wavespeed Model for the African Mantle Reveals Two Whole-Mantle Plumes Below East Africa and Neoproterozoic Modification of the Tanzania Craton. *Geochemistry, Geophysics, Geosystems*, *22*(3), 1–27. https://doi.org/10.1029/2020GC009302

Buck, W. R. (2006). The role of magma in the development of the Afro-Arabian Rift System. *Geological Society, London, Special Publications*, *259*(1), 43–54. https://doi.org/10.1144/GSL.SP.2006.259.01.05

Carbotte, S. M., Marjanović, M., Arnulf, A. F., Nedimović, M. R., Canales, J. P., & Arnoux, G. M. (2021). Stacked Magma Lenses Beneath Mid-Ocean Ridges: Insights From New Seismic Observations and Synthesis With Prior Geophysical and Geologic Findings. *Journal of Geophysical Research: Solid Earth*, *126*(4), 1–19. https://doi.org/10.1029/2020JB021434

Caricchi, L., Burlini, L., & Ulmer, P. (2008). Propagation of P and S-waves in magmas with different crystal contents : Insights into the crystallinity of magmatic reservoirs. *Journal of Volcanology and Geothermal Research*, *178*(4), 740–750. https://doi.org/10.1016/j.jvolgeores.2008.09.006

Cashman, K. V., Sparks, R. S. J., & Blundy, J. D. (2017). Vertically extensive and unstable magmatic systems: A unified view of igneous processes. *Science*, *355*(6331). https://doi.org/10.1126/science.aag3055

Chambers, E. L., Harmon, N., Keir, D., & Rychert, C. A. (2019). Using Ambient Noise to

Image the Northern East African Rift. *Geochemistry, Geophysics, Geosystems*, *20*, 2091–2109. https://doi.org/10.1029/2018GC008129

Chambers, E. L., Harmon, N., Rychert, C. A., & Keir, D. (2021). Variations in melt emplacement beneath the northern East African Rift from radial anisotropy. *Earth and Planetary Science Letters*, *573*, 117150. https://doi.org/10.1016/j.epsl.2021.117150

Civiero, C., Armitage, J. J., Goes, S., & Hammond, J. O. S. (2019). The Seismic Signature of Upper-Mantle Plumes: Application to the Northern East African Rift. *Geochemistry, Geophysics, Geosystems*, 1–17. https://doi.org/10.1029/2019GC008636

Civiero, C., Goes, S., Hammond, J. O. S., Fishwick, S., Ahmed, A., Ayele, A., … Stuart, Graham W. (2016). Small-scale thermal upwellings under the northern East African Rift from S travel time tomography. *Journal of Geophysical Research: Solid Earth*, *2010*, 1–14. https://doi.org/10.1002/2016JB013070.Received

Civiero, C., Hammond, J. O. S., Goes, S., Fishwick, S., Ahmed, A., Ayele, A., … Stuart, Graham W. (2015). Multiple mantle upwellings in the transition zone beneath the northern East-African Rift system from relative P-wave travel-time tomography. *Geochemistry, Geophysics, Geosystems*, *16*(9), 2949–2968. https://doi.org/10.1002/2015GC005948

Cornwell, D. G., Mackenzie, G. D., England, R. W., Maguire, P. K. H., Asfaw, L., & Oluma, B. (2006). Northern Main Ethiopian Rift crustal structure from new high-precision gravity data. *Geological Society, London, Special Publications*, *259*(1), 307–321. https://doi.org/10.1144/GSL.SP.2006.259.01.23

Cornwell, D. G., Maguire, P. K. H., England, R. W., & Stuart, G. W. (2010). Imaging detailed crustal structure and magmatic intrusion across the Ethiopian Rift using a dense linear broadband array. *Geochemistry, Geophysics, Geosystems*, *11*(1). https://doi.org/10.1029/2009GC002637

Corti, G. (2009). Continental rift evolution: From rift initiation to incipient break-up in the Main Ethiopian Rift, East Africa. *Earth-Science Reviews*, *96*(1–2), 1–53. https://doi.org/10.1016/j.earscirev.2009.06.005

Corti, G., Agostini, A., Keir, D., Van Wijk, J., Bastow, I. D., & Ranalli, G. (2015). Magma-induced axial subsidence during final-stage rifting: Implications for the development of seaward-dipping reflectors. *Geosphere*, *11*(3), 563–571. https://doi.org/10.1130/GES01076.1

Daly, E., Keir, D., Ebinger, C. J., Stuart, G. W., Bastow, I. D., & Ayele, A. (2008). Crustal tomographic imaging of a transitional continental rift : the Ethiopian rift. *Geophysical Journal International*, *172*, 1033–1048. https://doi.org/10.1111/j.1365-246X.2007.03682.x

Davidson, A., & Rex, D. C. (1980). Age of volcanism and rifting in southwestern Ethiopia. *Nature*, *283*(5748), 657–658. https://doi.org/10.1038/283657a0

Dugda, M. T., Nyblade, A. A., & Julia, J. (2007). Thin lithosphere beneath the Ethiopian Plateau revealed by a joint inversion of Rayleigh wave group velocities and receiver functions. *Journal of Geophysical Research: Solid Earth*, *112*(8), 1–14. https://doi.org/10.1029/2006JB004918

Dugda, M. T., Nyblade, A. A., Julia, J., Langston, C. A., Ammon, C. J., & Simiyu, S. (2005). Crustal structure in Ethiopia and Kenya from receiver function analysis : Implications for rift development in eastern Africa. *Journal of Geophysical Research*, *110*. https://doi.org/10.1029/2004JB003065

Dziewonski, A. M., & Anderson, D. L. (1981). Preliminary reference Earth model. *Physics of the Earth and Planetary Interiors*, *25*(4), 297–356. https://doi.org/10.1016/0031-9201(81)90046-7

Ebinger, C. J., & Casey, M. (2001). Continental breakup in magmatic provinces: An

Ethiopian example. *Geology*, *29*(6), 527–530.

Ebinger, C. J., Yemane, T., WoldeGabriel, G., Aronson, J. L., & C., W. R. (1993). Late Eocene-Recent volcanism and faulting in the southern main Ethiopian rift. *Journal of the Geological Society London*, *150*, 99–108.

Ferguson, D. J., MacLennan, J., Bastow, I. D., Pyle, D. M., Jones, S. M., Keir, D., … Yirgu, G. (2013). Melting during late-stage rifting in Afar is hot and deep. *Nature*, *499*(7456), 70–73. https://doi.org/10.1038/nature12292

Fischer, K. M., Rychert, C. A., Dalton, C. A., Miller, M. S., Beghein, C., & Schutt, D. L. (2020). A comparison of oceanic and continental mantle lithosphere. *Physics of the Earth and Planetary Interiors*, *309*(May), 106600. https://doi.org/10.1016/j.pepi.2020.106600

Fishwick, S. (2010). Surface wave tomography: Imaging of the lithosphere-asthenosphere boundary beneath central and southern Africa? *Lithos*, *120*(1–2), 63–73. https://doi.org/10.1016/j.lithos.2010.05.011

Forsyth, D. W., & Li, A. (2005). Array analysis of two-dimensional variations in surface wave phase velocity and azimuthal anisotropy in the presence of multipathing interference. *Seismic Earth: Array Analysis of Broadband Seismograms*, 81–97. https://doi.org/10.1029/157GM06

Furman, T., Nelson, W. R., & Elkins-Tanton, L. T. (2016). Evolution of the East African rift: Drip magmatism, lithospheric thinning and mafic volcanism. *Geochimica et Cosmochimica Acta*, *185*, 418–434. https://doi.org/10.1016/j.gca.2016.03.024

Gallacher, R. J., Keir, D., Harmon, N., Stuart, G. W., Leroy, S., Hammond, J. O. S., … Ahmed, A. (2016). The initiation of segmented buoyancy-driven melting during continental breakup. *Nature Communications*, *7*, 13110. https://doi.org/10.1038/ncomms13110

George, R., Rogers, N., & Kelley, S. P. (1998). Earliest magmatism in Ethiopia: Evidence for two mantle plumes in one flood basalt province. *Geology*, *26*(10), 923–926.

Goitom, B., Oppenheimer, C., Hammond, J. O. S., Grandin, R., Barnie, T. D., Donovan, A., … Berhe, S. (2015). First recorded eruption of Nabro volcano, Eritrea, 2011. *Bulletin of Volcanology*, *77*(10). https://doi.org/10.1007/s00445-015-0966-3

Hammond, J. O. S. (2014). Constraining melt geometries beneath the Afar Depression, Ethiopia from teleseismic receiver functions: The anisotropic H-k stacking technique. *Geochemistry, Geophysics, Geosystems*, *15*(4), 1316–1322. https://doi.org/10.1002/2013GC005186

Hammond, J. O. S., & Kendall, J.-M. (2016). Constraints on melt distribution from seismology: A case study in Ethiopia. In *Geological Society Special Publication* (Vol. 420, pp. 127–147). https://doi.org/10.1144/SP420.14

Hammond, J. O. S., Kendall, J.-M., Angus, D., & Wookey, J. (2010). Interpreting spatial variations in anisotropy: Insights into the Main Ethiopian Rift from SKS waveform modelling. *Geophysical Journal International*, *181*(3), 1701–1712. https://doi.org/10.1111/j.1365-246X.2010.04587.x

Hammond, J. O. S., Kendall, J.-M., Stuart, G. W., Ebinger, C. J., Bastow, I. D., Keir, D., … Wright, T. J. (2013). Mantle upwelling and initiation of rift segmentation beneath the Afar Depression. *Geology*, *41*(6), 635–638. https://doi.org/10.1130/G33925.1

Hammond, J. O. S., Kendall, J.-M., Stuart, G. W., Keir, D., Ebinger, C. J., Ayele, A., & Belachew, M. (2011). The nature of the crust beneath the Afar triple junction: Evidence from receiver functions. *Geochemistry, Geophysics, Geosystems*, *12*(12), 1–24. https://doi.org/10.1029/2011GC003738

Hammond, J. O. S., Kendall, J.-M., Wookey, J., Stuart, G. W., Keir, D., & Ayele, A. (2014). Differentiating flow, melt, or fossil seismic anisotropy beneath Ethiopia. *Geochemistry,*

Geophysics, *Geosystems*, *15*, 1878–1894. https://doi.org/10.1002/2013GC005185.Received

Harmon, N., De La Cruz, M. S., Rychert, C. A., Abers, G. A., & Fischer, K. M. (2013). Crustal and mantle shear velocity structure of Costa Rica and Nicaragua from ambient noise and teleseismic Rayleigh wave tomography. *Geophysical Journal International*, *195*(2), 1300–1313. https://doi.org/10.1093/gji/ggt309

Harmon, N., Forsyth, D. W., & Webb, S. C. (2007). Using ambient seismic noise to determine short-period phase velocities and shallow shear velocities in young oceanic lithosphere. *Bulletin of the Seismological Society of America*, *97*(6), 2009–2023. https://doi.org/10.1785/0120070050

Harmon, N., Gerstoft, P., Rychert, C. A., Abers, G. A., de la Cruz, M. S., & Fischer, K. M. (2008). Phase velocities from seismic noise using beamforming and cross correlation in Costa Rica and Nicaragua. *Geophysical Research Letters*, *35*(19), 1–6. https://doi.org/10.1029/2008GL035387

Harmon, N., Rychert, C. A., & Gerstoft, P. (2010). Distribution of noise sources for seismic interferometry. *Geophysical Journal International*, *183*(3), 1470–1484. https://doi.org/10.1111/j.1365-246X.2010.04802.x

Harmon, N., Rychert, C. A., Kendall, J.-M., Agius, M., Bogiatzis, P., & Tharimena, S. (2020). Evolution of the Oceanic Lithosphere in the Equatorial Atlantic From Rayleigh Wave Tomography, Evidence for Small-Scale Convection From the PI-LAB Experiment. *Geochemistry, Geophysics, Geosystems*, *21*(9). https://doi.org/10.1029/2020gc009174

Harmon, N., Wang, S., Rychert, C. A., Constable, Steven, & Kendall, J.-M. (2021). Shear velocity inversion guided by resistivity structure from the PI-LAB Experiment for integrated estimates of partial melt in the mantle. *Journal of Geophysical Research:*

Solid Earth. https://doi.org/10.1029/2021jb022202

Hebert, L. B., & Montési, L. G. J. (2010). Generation of permeability barriers during melt extraction at mid-ocean ridges. *Geochemistry, Geophysics, Geosystems*, *11*(12), 1–17. https://doi.org/10.1029/2010GC003270

Hofmann, C., Courtillot, V., Féraud, G., Rochette, P., Yirgu, G., Ketefo, E., & Pik, R. (1997). Timing of the ethiopian flood basalt event and implications for plume birth and global change. *Nature*, *389*(6653), 838–841. https://doi.org/10.1038/39853

Holtzman, B. K., & Kendall, J.-M. (2010). Organized melt, seismic anisotropy, and plate boundary lubrication. *Geochemistry, Geophysics, Geosystems*, *11*(12), 1–29. https://doi.org/10.1029/2010GC003296

Hübert, J., Whaler, K. A., & Fisseha, S. (2018). The Electrical Structure of the Central Main Ethiopian Rift as Imaged by Magnetotellurics : Implications for Magma Storage and Pathways. *Journal of Geophysical Research: Solid Earth*, *123*, 6019–6032. https://doi.org/10.1029/2017JB015160

Jackson, I., & Faul, U. H. (2010). Grainsize-sensitive viscoelastic relaxation in olivine: Towards a robust laboratory-based model for seismological application. *Physics of the Earth and Planetary Interiors*, *183*(1–2), 151–163. https://doi.org/10.1016/j.pepi.2010.09.005

Jestin, F., Huchon, P., & Gaulier, J. M. (1994). The Somalia Plate and the East-African Rift System - Present- Day Kinematics. *Geophysical Journal International*, *116*(3), 637–654.

Jin, G., Gaherty, J. B., Abers, G. A., Kim, Y., Eilon, Z. C., & Buck, W. R. (2015). Crust and upper mantle structure associated with extension in the Woodlark Rift, Papua New Guinea from Rayleigh-wave tomography. *Geochemistry, Geophysics, Geosystems*, *16*(1), 3808–3824. https://doi.org/10.1002/ 2015GC005840

Jones, P. W. (1976). Age of the lower flood basalts of the Ethiopian plateau. *Nature*,

261(5561), 567–569. https://doi.org/10.1038/261567a0

Keir, D., Bastow, I. D., Pagli, C., & Chambers, E. L. (2012). The development of extension and magmatism in the Red Sea rift of Afar. *Tectonophysics*, *607*, 98–114. https://doi.org/10.1016/j.tecto.2012.10.015

Keir, D., Bastow, I. D., Whaler, K. A., Daly, E., Cornwell, D. G., & Hautot, S. (2009). Lower crustal earthquakes near the Ethiopian rift induced by magmatic processes. *Geochemistry, Geophysics, Geosystems*, *10*(6), 1–10. https://doi.org/10.1029/2009GC002382

Keir, D., Belachew, M., Ebinger, C. J., Kendall, J.-M., Hammond, J. O. S., Stuart, G. W., … Rowland, J. V. (2011). Mapping the evolving strain field during continental breakup from crustal anisotropy in the Afar Depression. *Nature Communications*, *2*, 285–287. https://doi.org/10.1038/ncomms1287

Keir, D., Kendall, J.-M., Ebinger, C. J., & Stuart, G. W. (2005). Variations in late syn-rift melt alignment inferred from shear-wave splitting in crustal earthquakes beneath the Ethiopian rift. *Geophysical Research Letters*, *32*(23), 1–4. https://doi.org/10.1029/2005GL024150

Kendall, J.-M., Pilidou, S., Keir, D., Bastow, I. D., Stuart, G. W., & Ayele, A. (2006). Mantle upwellings , melt migration and the rifting of Africa : insights from seismic anisotropy. *Geological Society, London, Special Publications*, *259*, 55–72.

Kendall, J.-M., Stuart, G. W., Ebinger, C. J., Bastow, I. D., & Keir, D. (2005). Magma-assisted rifting in Ethiopia. *Nature*, *433*(7022), 146–148. https://doi.org/10.1038/nature03161

Kennett, B. L. N., Engdahl, E. R., & Buland, R. (1995). Constraints on seismic velocities in the Earth from traveltimes. *Geophysical Journal International*, *122*(1), 108–124. https://doi.org/10.1111/j.1365-246X.1995.tb03540.x

Keranen, K. M., Klemperer, S. L., Gloaguen, R., & EAGLE Working Group. (2004). Three-dimensional seismic imaging of a protoridge axis in the Main Ethiopian rift. *Geology*, *32*(11), 949–952. https://doi.org/10.1130/G20737.1

Keranen, K. M., Klemperer, S. L., Julia, J., Lawrence, J. F., & Nyblade, A. A. (2009). Low lower crustal velocity across Ethiopia: Is the Main Ethiopian Rift a narrow rift in a hot craton? *Geochemistry, Geophysics, Geosystems*, *10*(5). https://doi.org/10.1029/2008GC002293

Kieffer, B., Arndt, N. T., Lapierre, H., Bastien, F., Bosch, D., Pecher, A., … Meugniot, C. (2004). Flood and Shield Basalts from Ethiopia: Magmas from the African Superswell. *Journal of Petrology*, *45*(4), 793–834. https://doi.org/10.1093/petrology/egg112

Kim, S., Nyblade, A. A., Rhie, J., Baag, C.-E., & Kang, T.-S. (2012). Crustal S -wave velocity structure of the Main Ethiopian Rift from ambient noise tomography. *Geophysical Journal International*, *191*(2), 865–878. https://doi.org/10.1111/j.1365-246X.2012.05664.x

Koptev, A., Burov, E., Gerya, T., Le Pourhiet, L., Leroy, S., Calais, E., & Jolivet, L. (2018). Plume-induced continental rifting and break-up in ultra-slow extension context: Insights from 3D numerical modeling. *Tectonophysics*, *746*, 121–137. https://doi.org/10.1016/j.tecto.2017.03.025

Korostelev, F., Weemstra, C., Leroy, S., Boschi, L., Keir, D., Ren, Y., … Ayele, A. (2015). Magmatism on rift flanks: Insights from ambient noise phase velocity in Afar region. *Geophysical Research Letters*, *42*(7), 2179–2188. https://doi.org/10.1002/2015GL063259

La Rosa, A., Keir, D., Doubre, Cecile, Sani, F., Corti, G., Leroy, S., … Pagli, C. (2021). Lower Crustal Earthquakes in the March 2018 Sequence Along the Western Margin of Afar. *Geochemistry, Geophysics, Geosystems*, *22*(4), 1–15.

https://doi.org/10.1029/2020GC009614

Landisman, M., Dziewonski, A. M., & Satô, Y. (1969). Recent Improvements in the Analysis of Surface Wave Observations. *Geophysical Journal of the Royal Astronomical Society*, *17*, 369–403. https://doi.org/10.4294/jpe1952.16.Special_1

Laske, G., Masters, G., Ma, Z., & Pasyanos, M. E. (2013). Update on CRUST1.0 - A 1-degree global model of Earth's crust. *EGU General Assembly 2013*, *15*, 2658. Retrieved from http://meetingorganizer.copernicus.org/EGU2013/EGU2013-2658.pdf

Lavayssière, A., Rychert, C. A., Harmon, N., Keir, D., Hammond, J. O. S., Kendall, J.-M., … Leroy, Sylvie. (2018). Imaging lithospheric discontinuities beneath the northern East African Rift using S-to-P receiver functions. *Geochemistry, Geophysics, Geosystems*, *19*, 4048–4062.

Lekic, V., French, S. W., & Fischer, K. M. (2011). Lithospheric Thinning Beneath Rifted Regions of Southern California. *Science*, *334*(November), 783–788. https://doi.org/10.7551/mitpress/8876.003.0036

Ligi, M., Bonatti, E., Bortoluzzi, G., Cipriani, A., Cocchi, L., Caratori Tontini, F., … Schettino, A. (2012). Birth of an ocean in the Red Sea: Initial pangs. *Geochemistry, Geophysics, Geosystems*, *13*(8), 1–29. https://doi.org/10.1029/2012GC004155

Mackenzie, G. D., Thybo, H., & Maguire, P. K. H. (2005). Crustal velocity structure across the Main Ethiopian Rift: Results from two-dimensional wide-angle seismic modelling. *Geophysical Journal International*, *162*(3), 994–1006. https://doi.org/10.1111/j.1365-246X.2005.02710.x

Maguire, P. K. H., Keller, G. R., Klemperer, S. L., Mackenzie, G. D., Keranen, K. M., Harder, S., … Amha, M. (2006). Crustal structure of the northern Main Ethiopian Rift from the EAGLE controlled-source survey; a snapshot of incipient lithospheric break-up. *Geological Society, London, Special Publications*, *259*(1), 269–291.

https://doi.org/10.1144/GSL.SP.2006.259.01.21

Makris, J., & Ginzburg, A. (1987). The Afar Depression: transition between continental rifting and sea-floor spreading. *Tectonophysics*, *141*(1–3), 199–214. https://doi.org/10.1016/0040-1951(87)90186-7

McClusky, S., Reilinger, R., Ogubazghi, G., Amleson, A., Healeb, B., Vernant, P., … Kogan, L. (2010). Kinematics of the southern Red Sea – Afar Triple Junction and implications for plate dynamics. *Geophysical Research Letters*, *37*, 1–5. https://doi.org/10.1029/2009GL041127

Mège, D., & Korme, T. (2004). Dyke swarm emplacement in the Ethiopian Large Igneous Province: Not only a matter of stress. *Journal of Volcanology and Geothermal Research*, *132*(4), 283–310. https://doi.org/10.1016/S0377-0273(03)00318-4

Meshesha, D., & Shinjo, R. (2007). Crustal contamination and diversity of magma sources in the northwestern Ethiopian volcanic province. *Journal of Mineralogical and Petrological Sciences*, *102*(5), 272–290. https://doi.org/10.2465/jmps.061129

Muluneh, A. A., Keir, D., & Corti, G. (2021). Thermo-Rheological Properties of the Ethiopian Lithosphere and Evidence for Transient Fluid Induced Lower Crustal Seismicity Beneath the Ethiopian Rift. *Frontiers in Earth Science*, *9*(May). https://doi.org/10.3389/feart.2021.610165

Nishida, K. (2011). Two-dimensional sensitivity kernels for cross-correlation functions of background surface waves. *Comptes Rendus - Geoscience*, *343*(8–9), 584–590. https://doi.org/10.1016/j.crte.2011.02.004

Ogden, C. S., Bastow, I. D., Gilligan, A., & Rondenay, S. (2019). A Reappraisal of the H-κ Stacking Technique: Implications for Global Crustal Structure. *Geophysical Journal International*, *219*, 1491–1513. https://doi.org/10.1093/gji/ggz364

Petersen, K. D., Armitage, J. J., Nielsen, S. B., & Thybo, H. (2015). Mantle temperature as a

control on the time scale of thermal evolution of extensional basins. *Earth and Planetary Science Letters*, *409*, 61–70. https://doi.org/10.1016/j.epsl.2014.10.043

Pik, R., Deniel, C., Coulon, C., Yirgu, G., Hofmann, C., & Ayalew, D. (1998). The northwestern Ethiopian Plateau flood basalts: classification and spatial distribution of magma types. *Journal of Volcanology and Geothermal Research*, *81*(1–2), 91–111. https://doi.org/10.1016/S0377-0273(97)00073-5

Press, W. H., Teukolsky, S. A., Vetterling, W. T., & Flannery, B. P. (1992). Press. In *Numerical recipes in C: The art of scientific computing* (Second edn, pp. 444–455). Cambridge University Press.

Rooney, T. O. (2017). The Cenozoic magmatism of East-Africa: Part I — Flood basalts and pulsed magmatism. *Lithos*, *286–287*, 264–301. https://doi.org/10.1016/j.lithos.2017.05.014

Rooney, T. O. (2019). The Cenozoic Magmatism of East Africa: Part V – Magma sources and Processes in the East African Rift. *Lithos*. https://doi.org/10.1016/j.ctim.2019.102211

Rooney, T. O. (2020). The Cenozoic magmatism of East Africa: Part IV – The terminal stages of rifting preserved in the Northern East African Rift System. *Lithos*, *360–361*, 105381. https://doi.org/10.1016/j.lithos.2020.105381

Rooney, T. O., Bastow, I. D., Keir, D., Mazzarini, F., Movsesian, E., Grosfils, E. B., … Yirgu, G. (2014). The protracted development of focused magmatic intrusion during continental rifting. *Tectonics*, *33*, 875–897. https://doi.org/10.1002/2013TC003514.Received

Rooney, T. O., Furman, T., Yirgu, G., & Ayalew, D. (2005). Structure of the Ethiopian lithosphere: Xenolith evidence in the Main Ethiopian Rift. *Geochimica et Cosmochimica Acta*, *69*(15), 3889–3910. https://doi.org/10.1016/j.gca.2005.03.043

Rooney, T. O., Hanan, B. B., Graham, D. W., Furman, T., Blichert-toft, J., & Schilling, J. G. (2012). Upper mantle pollution during Afar plume-continental rift interaction. *Journal of Petrology*, *53*(2), 365–389. https://doi.org/10.1093/petrology/egr065

Rooney, T. O., Herzberg, C., & Bastow, I. D. (2012). Elevated mantle temperature beneath East Africa. *Geology*, *40*(1), 27–30. https://doi.org/10.1130/G32382.1

Rychert, C. A., Fischer, K. M., & Rondenay, S. (2005). A sharp lithosphere – asthenosphere boundary imaged beneath eastern North America. *Nature*, *436*, 542–545. https://doi.org/10.1038/nature03904

Rychert, C. A., Hammond, J. O. S., Harmon, N., Kendall, J.-M., Keir, D., Ebinger, C. J., … Stuart, G. W. (2012). Volcanism in the Afar Rift sustained by decompression melting with minimal plume influence. *Nature Geoscience*, *5*(6), 406–409. https://doi.org/10.1038/ngeo1455

Rychert, C. A., & Harmon, N. (2018). Predictions and Observations for the Oceanic Lithosphere From S-to-P Receiver Functions and SS Precursors. *Geophysical Research Letters*, *45*(11), 5398–5406. https://doi.org/10.1029/2018GL077675

Rychert, C. A., Harmon, N., Constable, Steve, & Wang, S. (2020). The nature of the Lithosphere-Asthenosphere Boundary. *Journal of Geophysical Research: Solid Earth*, 1–39. https://doi.org/10.1029/2018jb016463

Rychert, C. A., Tharimena, S., Harmon, N., Wang, S., Constable, Steven, Kendall, J.-M., … Schlaphorst, D. (2021). A dynamic lithosphere–asthenosphere boundary near the equatorial Mid-Atlantic Ridge. *Earth and Planetary Science Letters*, *566*, 116949. https://doi.org/10.1016/j.epsl.2021.116949

Saito, M. (1988). DISPER80: a subroutine package for the calculation of seismic normal-mode solutions. In D. J. Doornbos (Ed.), *Seismological Algorithms: Computational Methods and Computer Programs* (pp. 293–319). Academic Press.

Samrock, F., Grayver, A. V., Eysteinsson, H., & Saar, M. O. (2018). Magnetotelluric Image of Transcrustal Magmatic System Beneath the Tulu Moye Geothermal Prospect in the Ethiopian Rift. *Geophysical Research Letters*, *45*(23), 12,847-12,855. https://doi.org/10.1029/2018GL080333

Sandwell, D., & Fialko, Y. (2004). Warping and cracking of the Pacific plate by thermal contraction. *Journal of Geophysical Research: Solid Earth*, *109*(10), 1–12. https://doi.org/10.1029/2004JB003091

Saria, E., Calais, E., Stamps, D. S., Delvaux, D., & Hartnady, C. (2014). Present-day kinematics of the East African Rift. *Journal of Geophysical Research: Solid Earth*, 1–17. https://doi.org/10.1002/2013JB010901.Received

Sim, S. J., Spiegelman, M., Stegman, D. R., & Wilson, C. (2020). The influence of spreading rate and permeability on melt focusing beneath mid-ocean ridges. *Physics of the Earth and Planetary Interiors*, *304*. https://doi.org/10.1016/j.pepi.2020.106486

Smith, M. (1994). Stratigraphic and structural constraints on mechanisms of active rifting in the Gregory Rift, Kenya. *Tectonophysics*, *236*(1–4), 3–22. https://doi.org/10.1016/0040-1951(94)90166-X

Sparks, D. W., & Parmentier, E. M. (1991). Melt extraction from the mantle beneath spreading centers. *Earth and Planetary Science Letters*, *105*(4), 368–377. https://doi.org/10.1016/0012-821X(91)90178-K

Stuart, G. W., Bastow, I. D., & Ebinger, C. J. (2006). Crustal structure of the northern Main Ethiopian Rift from receiver function studies. *Geological Society, London, Special Publications*, *24*(4), 623–626. https://doi.org/10.1144/GSL.SP.2006.259.01.20

Tarantola, A., & Valette, B. (1982). Generalized nonlinear inverse problems solved using the least squares criterion. *Reviews of Geophysics*, *20*(2), 219–232. https://doi.org/10.1029/RG020i002p00219

Tesfaye, S., Harding, D. J., & Kusky, T. M. (2003). Early continental breakup boundary and migration of the Afar triple junction, Ethiopia. *Bulletin of the Geological Society of America*, *115*(9), 1053–1067. https://doi.org/10.1130/B25149.1

Tromp, J., Luo, Y., Hanasoge, S. M., & Peter, D. (2010). Noise cross-correlation sensitivity kernels. *Geophysical Journal International*, *183*(2), 791–819. https://doi.org/10.1111/j.1365-246X.2010.04721.x

Ukstins, I. A., Renne, P. R., Wolfenden, E., Baker, J., Ayalew, D., & Menzies, M. (2002). Matching conjugate volcanic rifted margins: 40Ar/39Ar chrono-stratigraphy of pre- and syn-rift bimodal flood volcanism in Ethiopia and Yemen. *Earth and Planetary Science Letters*, *198*(3–4), 289–306. https://doi.org/10.1016/S0012-821X(02)00525-3

Vigny, C., Huchon, P., Ruegg, J., Khanbari, K., & Asfaw, L. (2006). Confirmation of Arabia plate slow motion by new GPS data in Yemen. *Journal of Geophysical Research*, *111*(April 2005), 1–14. https://doi.org/10.1029/2004JB003229

Wang, S., Constable, Steven, Rychert, C. A., & Harmon, N. (2020). A Lithosphere-Asthenosphere Boundary and Partial Melt Estimated Using Marine Magnetotelluric Data at the Central Middle Atlantic Ridge. *Geochemistry, Geophysics, Geosystems*, *21*(9), 1–7. https://doi.org/10.1029/2020GC009177

Wang, T., Gao, S. S., Yang, Q., & Liu, K. H. (2021). Crustal structure beneath the Ethiopian Plateau and adjacent areas from receiver functions: Implications for partial melting and magmatic underplating. *Tectonophysics*. https://doi.org/10.1016/j.tecto.2021.228857

Wang, Y., Forsyth, D. W., & Savage, B. (2009). Convective upwelling in the mantle beneath the Gulf of California. *Nature*, *462*(7272), 499–501. https://doi.org/10.1038/nature08552

Wessel, P., Smith, W. H. F., Scharroo, R., Luis, J., & Wobbe, F. (2013). Generic mapping tools: Improved version released. *Eos*, *94*(45), 409–410. https://doi.org/10.1002/2013EO450001

Whaler, K. A., & Hautot, S. (2006). The electrical resistivity structure of the crust beneath the northern Main Ethiopian Rift. *Geological Society, London, Special Publications*, *259*, 293–305.

Wolfenden, E., Ebinger, C. J., Yirgu, G., Deino, A., & Ayalew, D. (2004). Evolution of the northern Main Ethiopian rift: birth of a triple junction. *Earth and Planetary Science Letters*, *224*(1–2), 213–228. https://doi.org/10.1016/j.epsl.2004.04.022

Wolfenden, E., Ebinger, C. J., Yirgu, G., Renne, P. R., & Kelley, S. P. (2005). Evolution of a volcanic rifted margin: Southern Red Sea, Ethiopia. *Bulletin of the Geological Society of America*, *117*(7–8), 846–864. https://doi.org/10.1130/B25516.1

Yang, Y., & Forsyth, D. W. (2006). Regional tomographic inversion of the amplitude and phase of Rayleigh waves with 2-D sensitivity kernels. *Geophysical Journal International*, *166*(3), 1148–1160. https://doi.org/10.1109/TIM.2006.876410

Yao, H., & van der Hilst, R. D. (2009). Analysis of ambient noise energy distribution and phase velocity bias in ambient noise tomography, with application to SE Tibet. *Geophysical Journal International*, *179*(2), 1113–1132. https://doi.org/10.1111/j.1365-246X.2009.04329.x

Yoshizawa, K., & Kennett, B. L. N. (2002). Determination of the influence zone for surface wave paths. *Geophysical Journal International*, *149*(2), 440–453. https://doi.org/10.1046/j.1365-246X.2002.01659.x

Zhou, Y., Dahlen, F. A., & Nolet, G. (2004). Three-dimensional sensitivity kernels for surface wave observables. *Geophysical Journal International*, *158*(1), 142–168. https://doi.org/10.1111/j.1365-246X.2004.02324.x

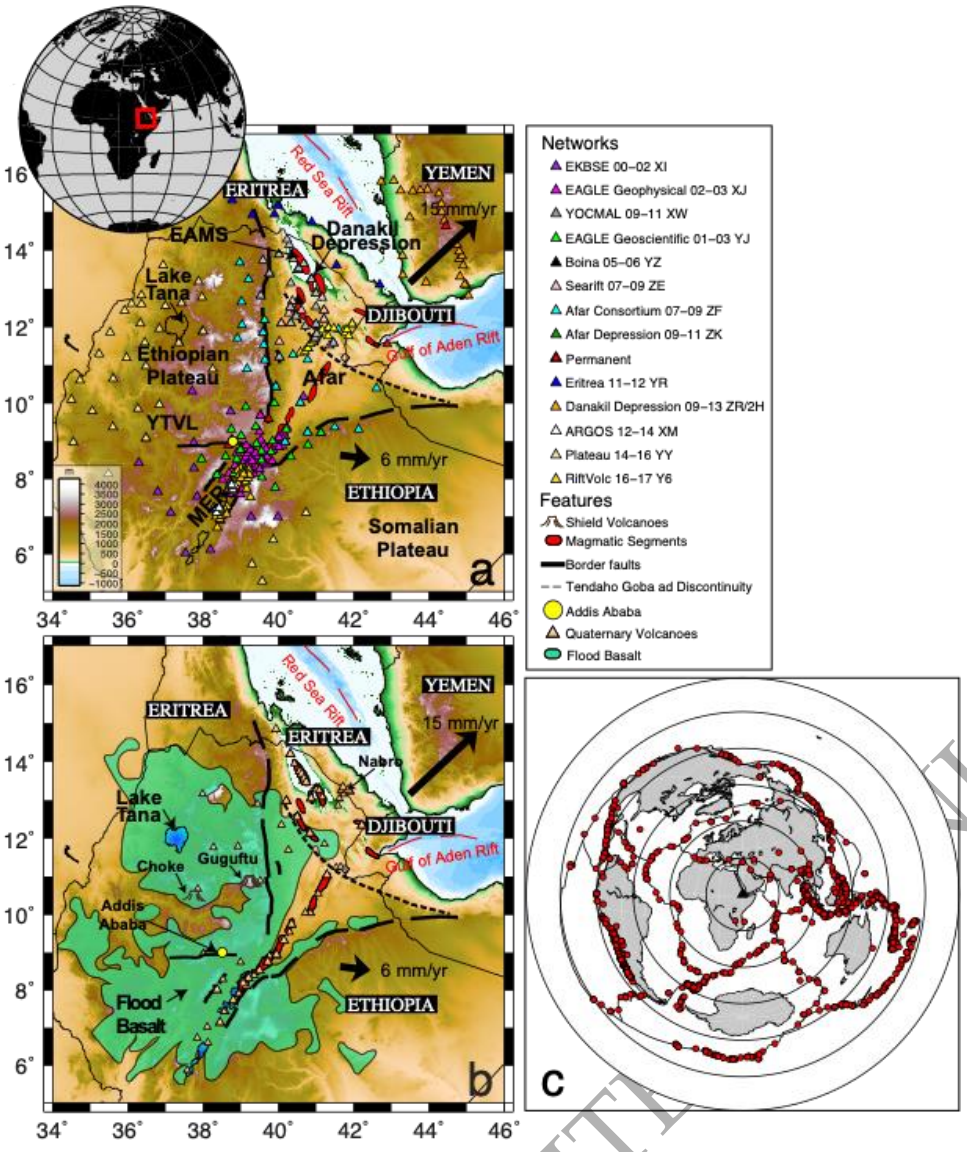

Figure 1a) Seismic station map of the northern East African Rift. Thick black lines show border faults, red polygons crustal magmatic segments (Keir et al., 2011)*, and thin dashed lines the Tendaho-Goba'ad discontinuity (TGD). Yerer Tullu Wellel Volcanotectonic lineament is marked by YTVL and thick black line. Seismic stations are triangles and are coloured by their project deployment with the final 4 networks (Danakil depression–RiftVolc) new networks not previously used for ambient noise tomography. Arrows indicate extension rates relative to the stationary Nubian plate* (Jestin et al., 1994; Saria et al., 2014; Vigny et al., 2006). *b) Key feature map showing the location of Quaternary volcanoes (taken from the Global Volcanism Program, Smithsonian Institution, https://volcano.si.edu) represented by gradient filled inverted orange triangles. Shield volcanoes from the Miocene are represented by brown volcanoes* (Kieffer et al., 2004). *Flood basalt provinces are shown in blue and are mapped from* Mège & Korme (2004). *Addis Ababa is marked by a yellow circle. c) Red dots show the locations of the 1053 earthquakes from 1999-2017, with magnitude >5.5, used in this study.*

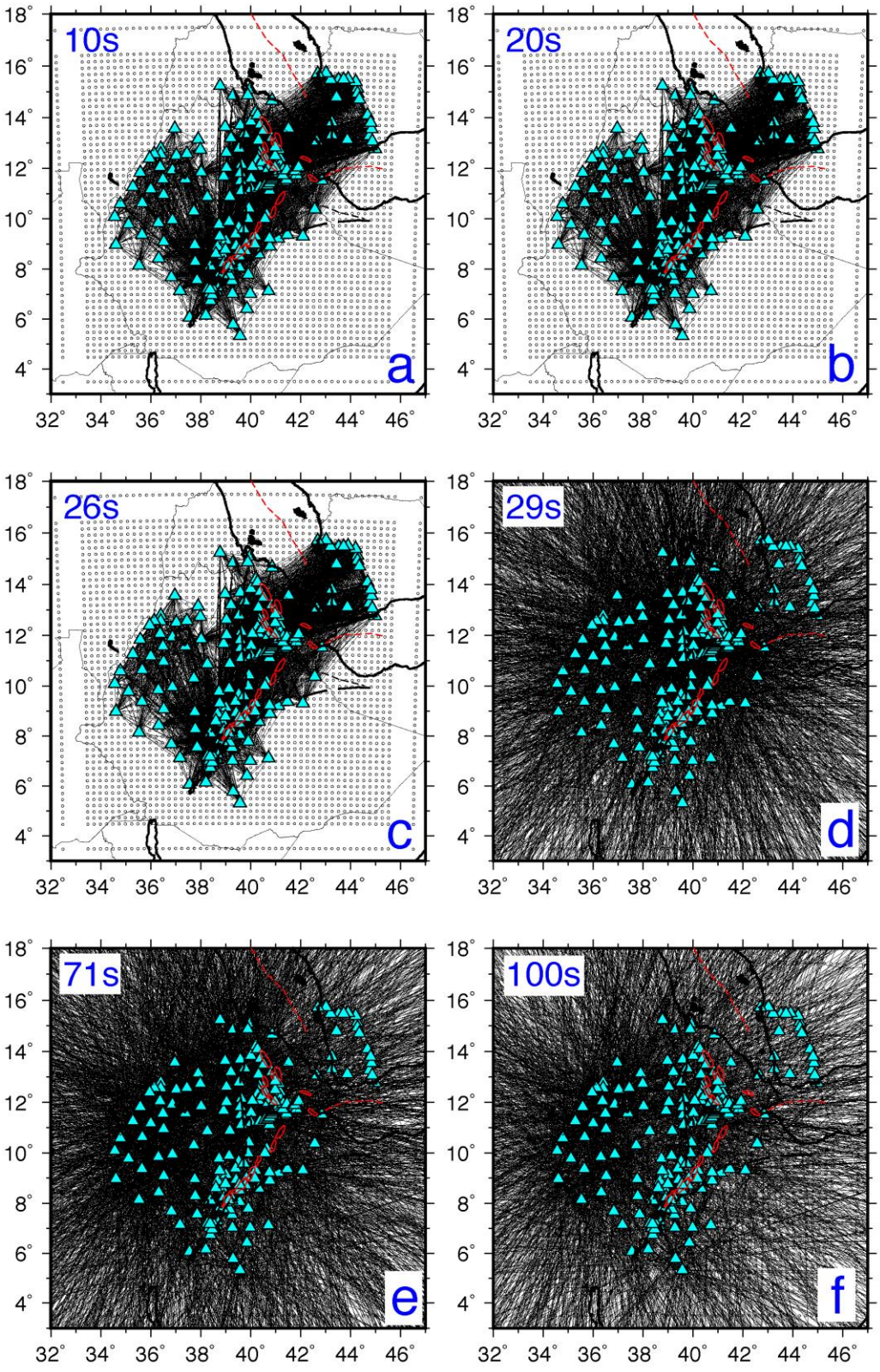

Figure 2 Nodal grid at 0.25 ° spacing with ray paths for ambient noise (a–c, 10, 20 and 26s) and teleseisms (d–f, 29, 71 and 100 s) overlain as black lines. Blue triangles indicate stations and red polygons the crustal magmatic segments.

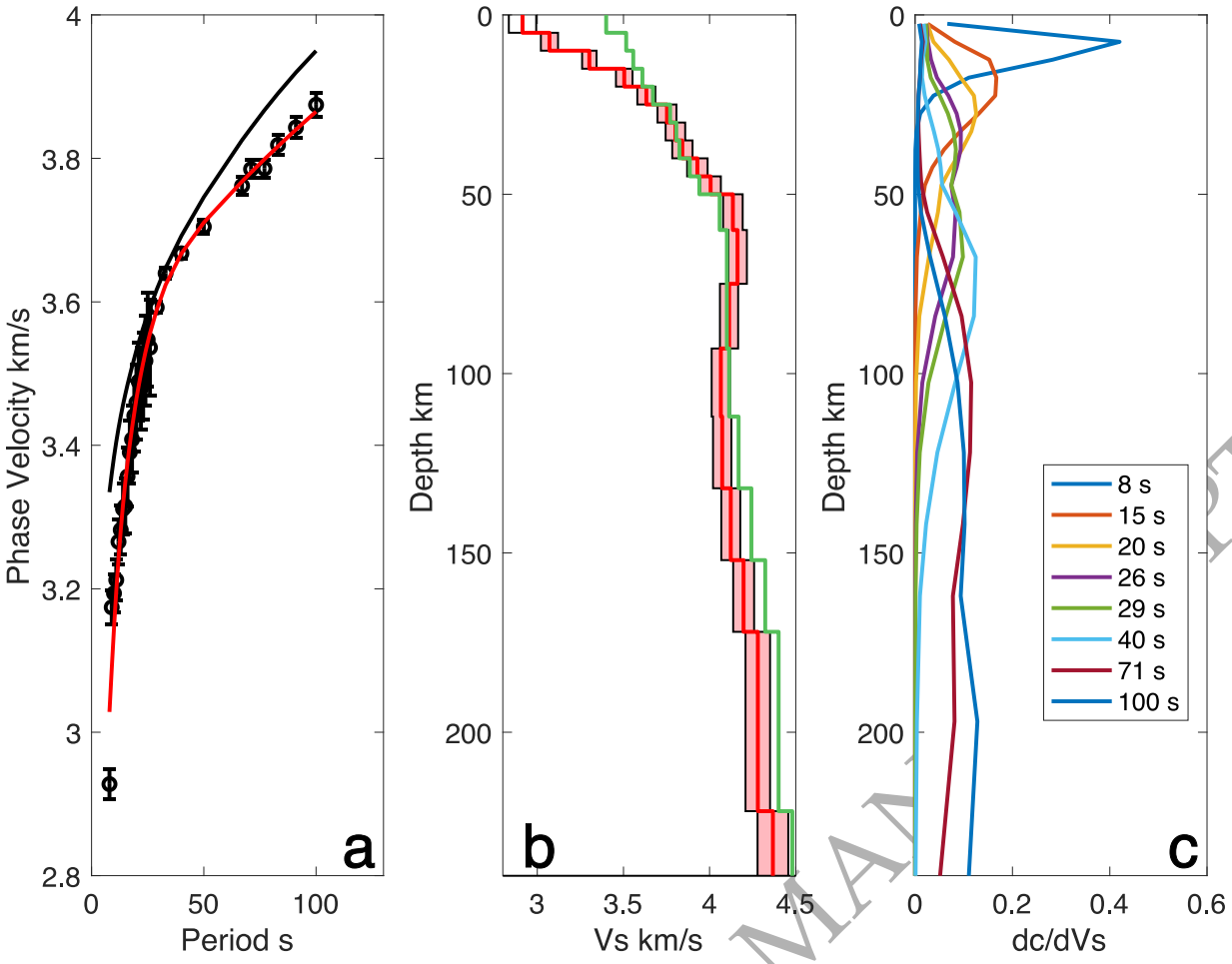

Figure 3a) Average 1-D phase velocity for the study area with 3σ error bars (circles), starting model (black line) with our best fit shear velocity model dispersion overlain (red line). (b) Best fit shear velocity model for the study area (red line) and formal 2σ error bounds (thin black lines and shaded area). Green line is initial starting model using the average shear velocity from Chambers et al., (2019) and Gallacher et al., (2016). (c) Sensitivity kernels for Rayleigh waves at selected periods.

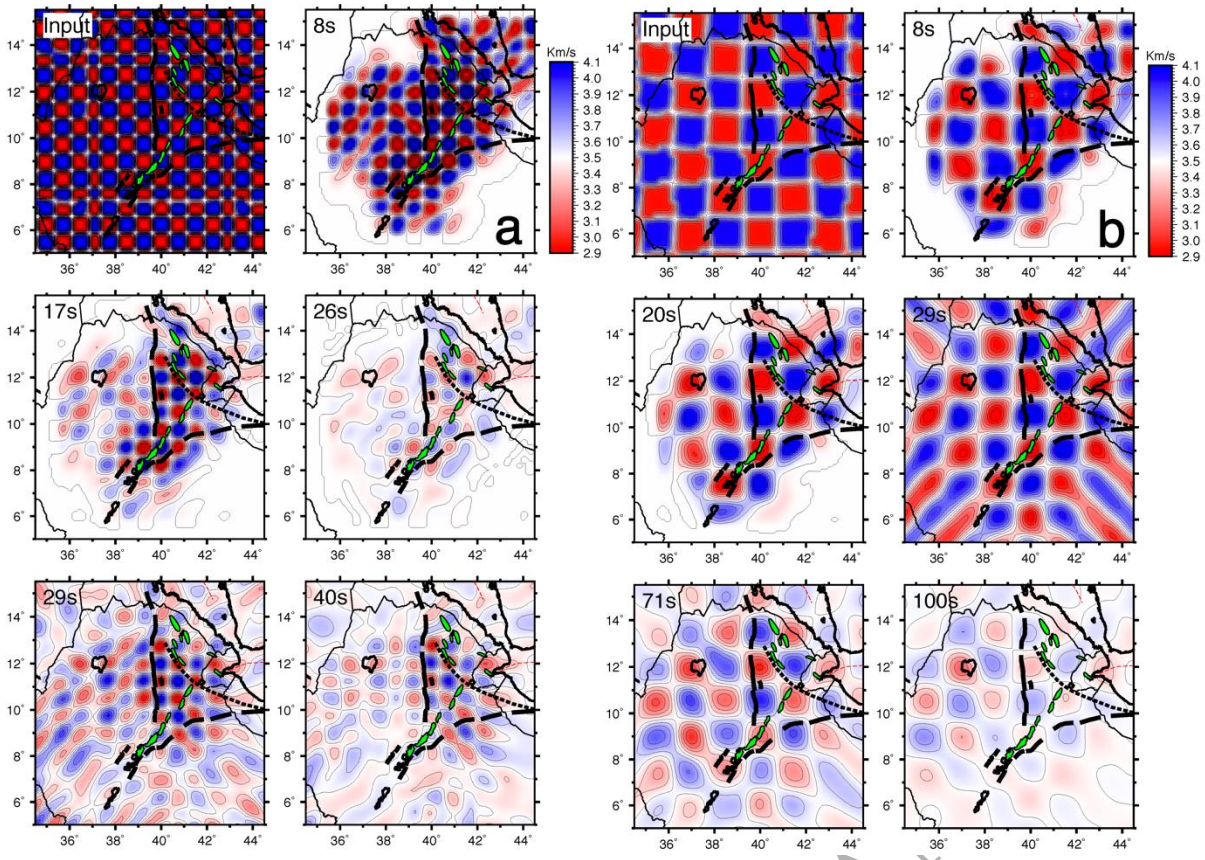

Figure 4 a) Checkerboard tests at 70 km × 70 km for phase velocities from ambient noise (8–26s) and teleseisms (29 and 40 s) which are sensitive to crustal and upper most mantle depths (left 2 panels). Within the rift and eastern part of the Ethiopian Plateau we can resolve the checkerboards with confidence. Outside these areas features should not be interpreted. Right 2 panels: b) Checkerboard tests at 165 km × 165 km (~1.5° x 1.5°) for phase velocities from ambient noise (8–20 s) and Teleseisms (29-100 s) for the minimum and maximum periods. Within the rift and eastern part of the Ethiopian Plateau we can resolve the checkerboards with confidence to 100 s period, although the magnitude of the anomaly weakens with increasing period. Thick black lines show border faults, green polygons crustal magmatic segments, and dashed lines the Tendaho-Goba'ad discontinuity (TGD). For further checker board tests at 110 km and 220 km spacings see supplementary Figures S7 and S8.

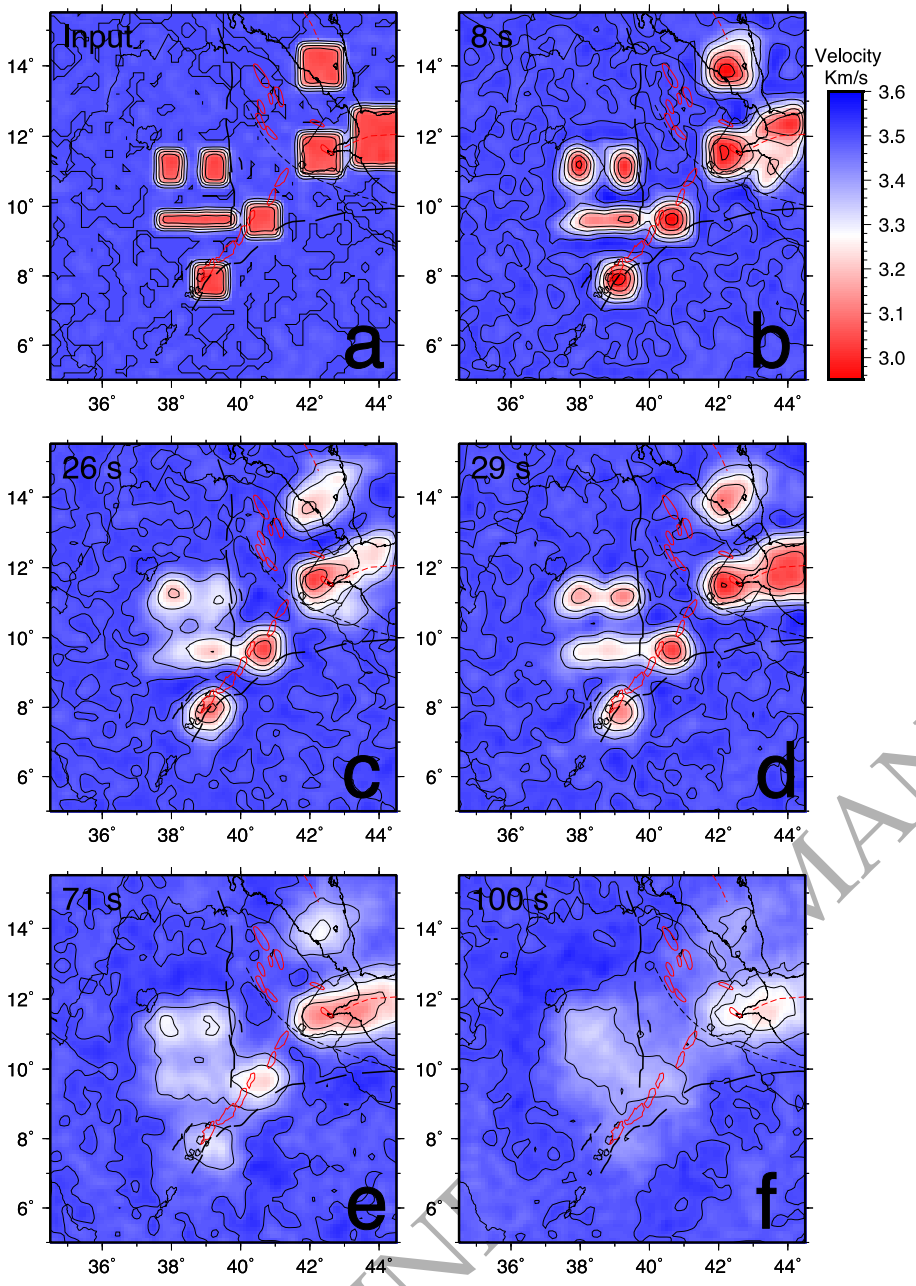

Figure 5 Synthetic recovery tests with 10% background noise added, inputting slow velocity anomalies beneath the Main Ethiopian Rift, YTVL, Red Sea Rift, Gulf of Aden Rift and beneath the eastern part of the Ethiopian Plateau at 8, 26, 29, 71 and 100 s period. Thick black lines show border faults, red polygons crustal magmatic segments, and dashed lines the Tendaho-Goba'ad discontinuity (TGD). Off-rift features are resolvable at short periods equivalent to crustal depths though smear together at longer periods. The MER and Gulf of Aden anomalies are visible at all periods with decreasing amplitude at longer periods with discrete slow velocity anomalies visible to 71s. Additional synthetic recovery tests are shown in Figure S9 for larger anomalies and a continuous slow velocity rift.

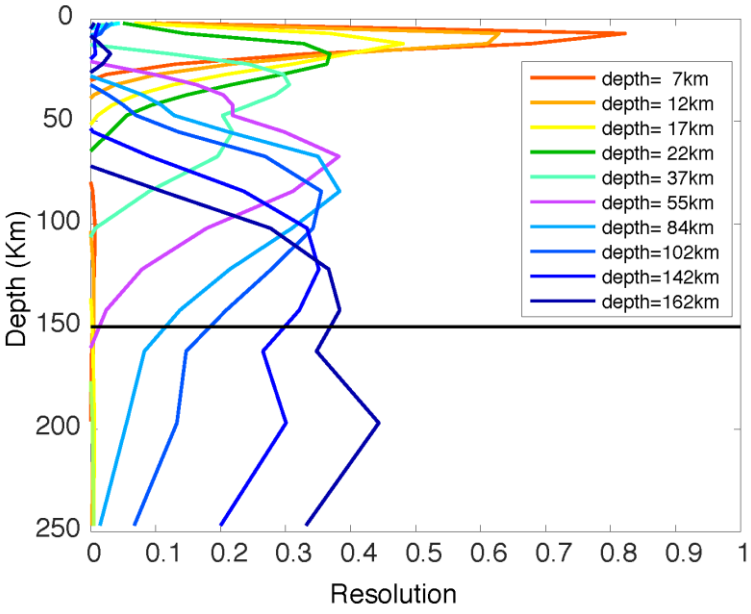

Figure 6 Spike test for depths of 7, 12, 17, 22, 37, 55, 84, 102, 142 and 162 km depth. Vertical resolution ranges from ±10 km at the shallowest depths (7-22 km) but includes a broader depth range for the deepest slices at 142-162 km depth.

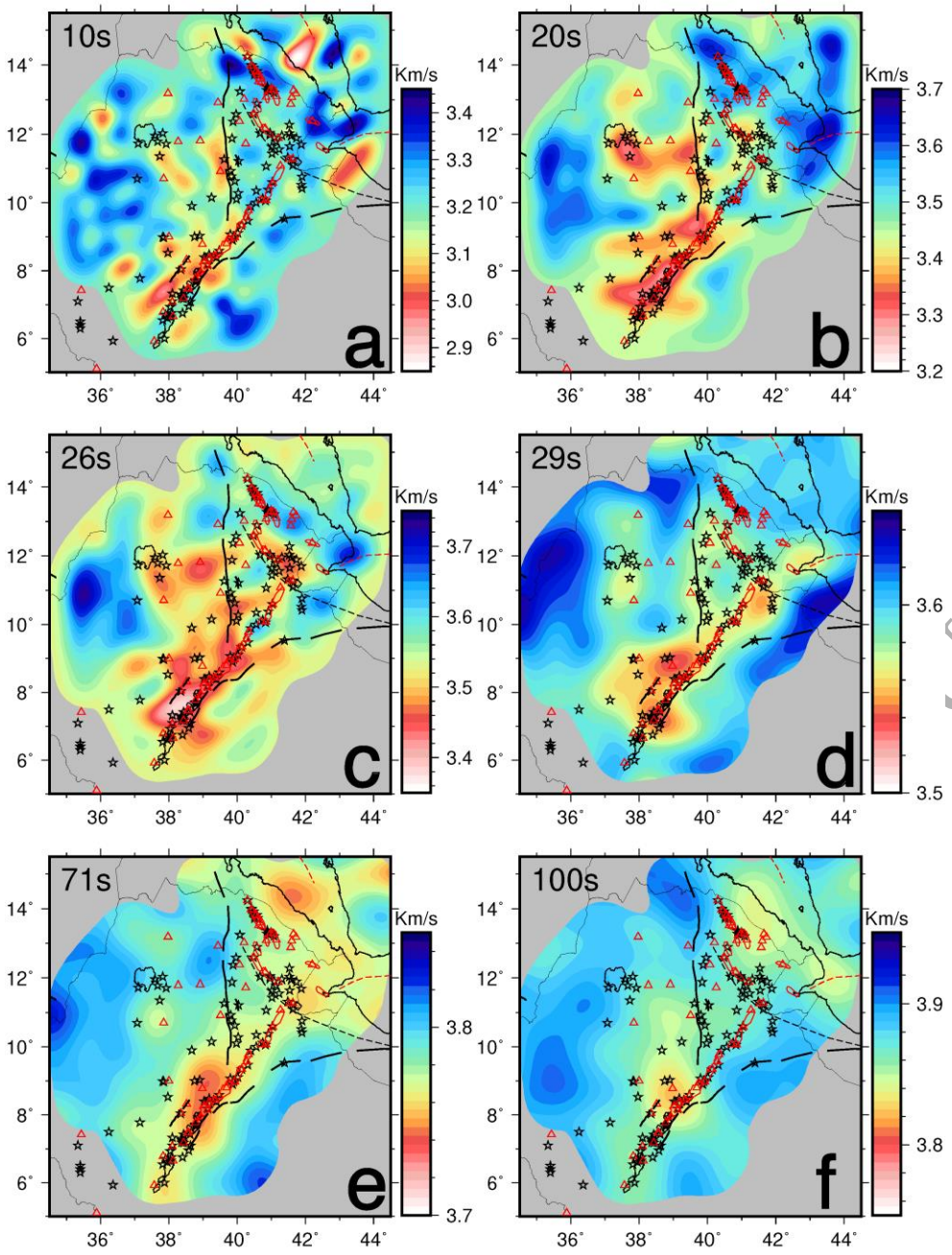

Figure 7 Phase velocity maps generated by tomographically inverting dispersion curves from ambient noise (10, 20, 26s) and teleseisms (29, 71 and 100 s). Models have been cropped to the 2σ standard error contour. Pink and red colours are slower velocities and blue faster velocities. Thick black lines indicate border faults, red polygons crustal magmatic segments, dashed lines the Tendaho-Goba'ad discontinuity (TGD), red triangles volcanoes, and black stars geothermal activity.

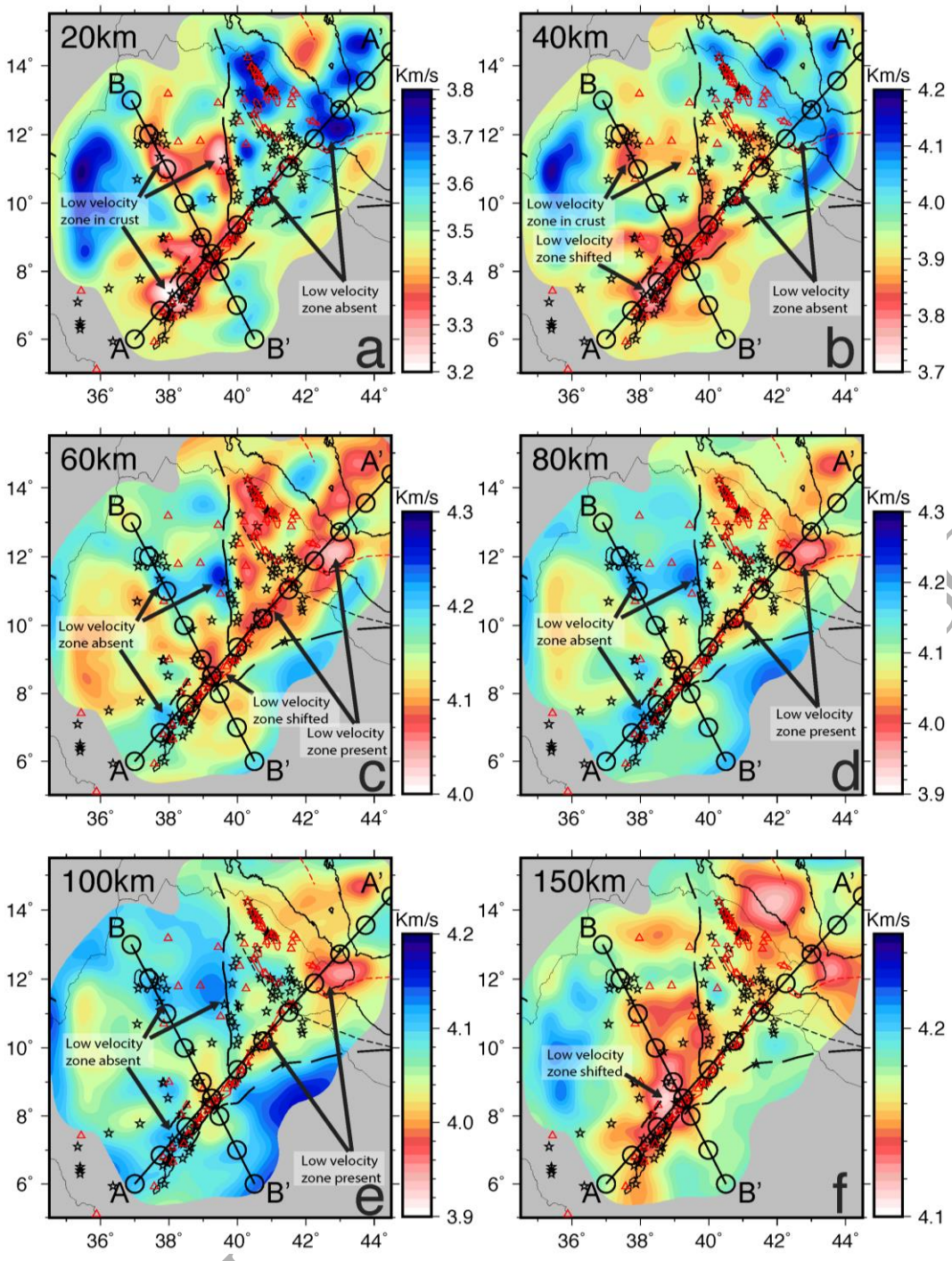

Figure 8 Interpolated absolute shear wave velocity at 20, 40, 60, 80, 100 and 150 km. Models have been cropped to the standard error contour. Pink and red colours indicates slower velocities and blue faster velocities. Thick black lines indicate border faults. 2 profiles (thin black lines with black rings) are the cross-section locations for Figure 9. Red polygons indicate crustal magmatic segments, red triangles volcanoes, and black stars geothermal activity. Arrows indicate areas discussed in the text. See supplementary Figure S11 for slices at 10 km depth intervals and fixed colour scales from 60 km – 150 km depth.

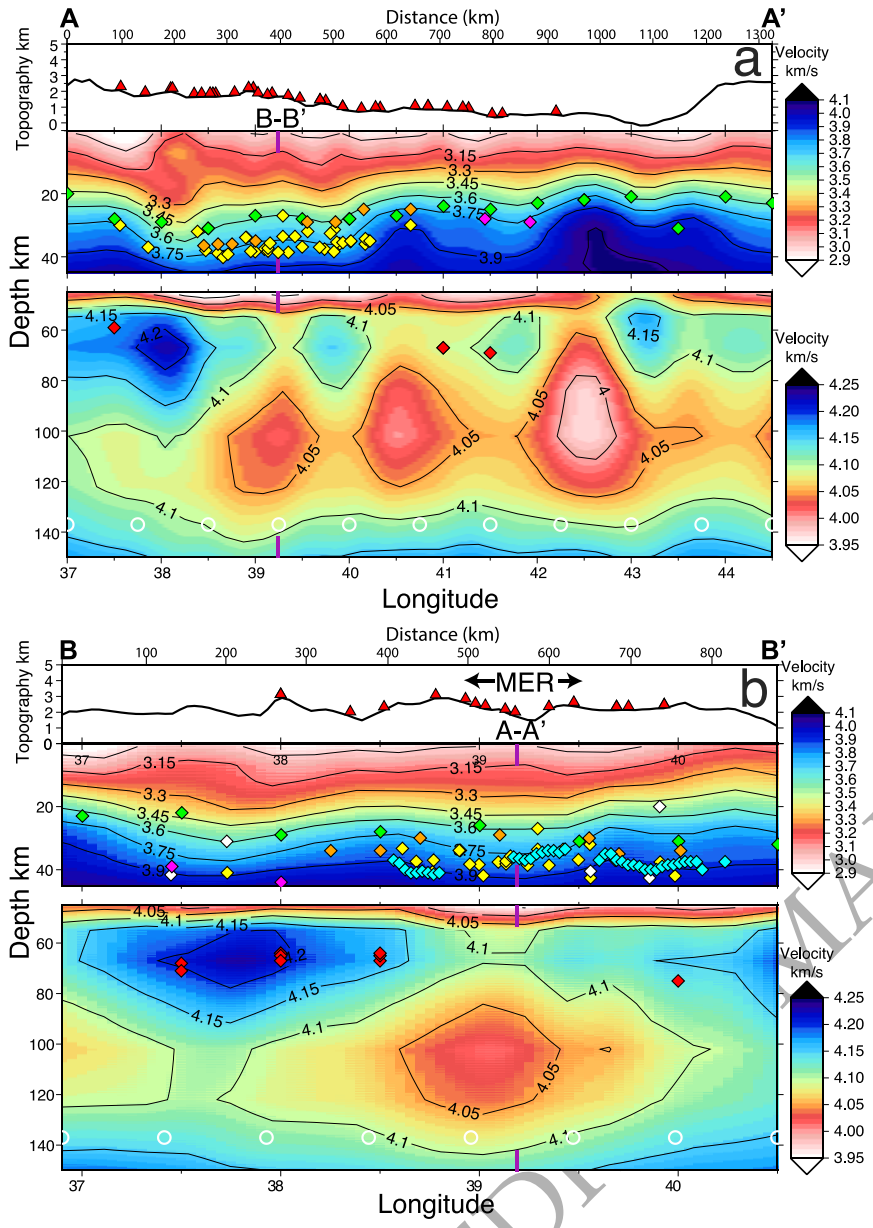

Figure 9 Cross-sections through the interpolated absolute shear velocity depth slices a) along the rift and b) across the rift (See Figure 8 for *locations). The cross-sections have been split into crustal section (0-45 km depth, top panel) and mantle (45–150 km depth, bottom panel) for display purposes. Red and pink colours indicate slower velocities, and blue faster velocities. Red triangles above section indicate quaternary volcanoes with topography as black line. Thin lines are velocity contours and diamonds represent previous receiver function results for the Moho in top sections (green* (Lavayssière et al., 2018), *magenta* (Hammond, et al., 2011), *yellow* (Stuart et al., 2006), *Orange* (Maguire et al., 2006), *Cyan* (Cornwell et al., 2010), *white* (Ogden et al., 2019)*) and LAB in bottom sections (red* (Lavayssière et al., 2018)*). White rings are the same as black rings in Figure 8, for location reference, and purple tick marks indicate the crossing points of A-A' and B-B' on the respective figures.*